Final Report

Project Title:	Carbon Dioxide Shuttling Thermochemical Storage Using Strontium Carbonate
Project Period:	(05/01/14 – 04/30/15)
Submission Date:	(06/15/15)
Recipient:	University of Florida
Address:	Mechanical and Aerospace Engineering, University of Florida 231 MAE-A Building P.O. Box 116250 Gainesville, FL 32611-6250
Website (if available)	www.mae.ufl.edu
Award Number:	DE-EE0006534
Project Team:	University of Florida Solar Fuel Corporation Siemens Corporation, Corporate Technology
Principal Investigator:	Renwei Mei, Professor Phone: 352-392-0888 Email: rwmei@ufl.edu
Business Contact:	Lisa Stroud Phone: 352-392-9447 Ext. 3 Email: lstroud@eng.ufl.edu
HQ Tech Manager:	Abraham Shultz, Levi Irwin
HQ Project Officer:	Tommy Rueckert
GO Grant Specialist:	Fania Gordon
GO Contracting Officer:	Uriel Trujillo

Executive Summary:

Phase I concludes with significant progress made towards the SunShot ELEMENTS goals of high energy density, high power density, and high temperature by virtue of a $SrO/SrCO_3$ based material. A detailed exploration of sintering inhibitors has been conducted and relatively stable materials supported by YSZ or $SrZO_3$ have been identified as the leading candidates. In 15 cycle runs using a 3 hour carbonation duration, several materials demonstrated energy densities of roughly 1500 MJ/m^3 or greater. The peak power density for the most productive materials consistently exceeded 40 MW/m^3—an order of magnitude greater than the SOPO milestone. The team currently has a material demonstrating nearly 1000 MJ/m^3 after 100 abbreviated (1 hour carbonation) cycles. A subsequent 8 hour carbonation after the 100 cycle test exhibited over 1500 MJ/m^3, which is evidence that the material still has capacity for high storage albeit with slower kinetics.

Kinetic carbonation experiments have shown three distinct periods: induction, kinetically-controlled, and finally a diffusion-controlled period. In contrast to thermodynamic equilibrium prediction, higher carbonation temperatures lead to greater conversions over a 1 hour periods, as diffusion of CO_2 is more rapid at higher temperatures. A polynomial expression was fit to describe the temperature dependence of the linear kinetically-controlled regime, which does not obey a traditional Arrhenius relationship. Temperature and CO_2 partial pressure effects on the induction period were also investigated. The CO_2 partial pressure has a strong effect on the reaction progress at high temperatures but is insignificant at temperatures under 900°C.

Tomography data for porous $SrO/SrCO_3$ structures at initial stage and after multiple carbonation/decomposition cycles have been obtained. Both 2D slices and 3D reconstructed representations have been obtained from the raw data. Porosity and surface area have been computed based on tomography. The two parameters, permeability and Forchheimer constants, in the Darcy's law for linear and non-linear range have been obtained from the fluid dynamics simulation. The structure is nearly isotropic from the hydrodynamics point of view. Thermal conductivity at elevated temperature has been obtained from the 3-D pore-scale simulations. The computed thermal conductivities of the structure compare well with an existing correlation. Computational models have been developed for solving the energy and mass transport equations with chemical reaction on the surface and inside the particles. The chemical kinetics or rate law is needed on the particle scale; however it is generally measured using a lumped model based on the average of reacted as well as unreacted mass. Many simulations have been conducted on a 2-D model to determine the effects of those pore scale parameters on the heat release based on the measured data. The simulation results using 2-D model show that average volumetric heat flow rate of 4 MW/m^3 in the first 5 minutes can be obtained. The insight gained from the 2-D simulation will be useful for the next stage simulation based on realistic 3-D structures.

A probabilistic analysis has been conducted on the baseline system of recovering heat from the hot CO_2 evolved from the endothermic reaction and compressing the cooled CO_2 into a storage tank at 20-21 bar. Using a Monte Carlo simulation using 2,000,000 samples and both uniform and triangular probability distributions of four variables (heat exchanger pinch points, compressor efficiency, and power block efficiency), exergetic efficiency of 90% appears to be very likely.

Table of Contents

Background 4
Introduction 5
Project Results and Discussion 9
Task 1.1: TGA and Longevity Tests 9
Task 1.2: Carbonation Kinetics 21
Task 1.3. De-carbonation Kinetics 29
Task 1.4: Direct Pore-Level Model 31
Task 1.5: Process Flowsheet 44
Task 1.6: Technology to Market 52
Conclusions 54
Budget and Schedule 54
Path Forward 55
References 56

Background:

Concentrated solar power (CSP) converts solar energy to heat before transformation to electrical energy, potentially allowing for more cost-effective storage. A CSP plant with storage offers dispatchable renewable power, allowing for high plant utilization since it can provide energy for load shifting or spinning reserves — essentially power on-demand. Although promising, thermal energy storage subsystems are cost-prohibitive. Greater volumetric energy storage density is therefore desired to bring down capital costs. Thermochemical energy storage (TCES) offers a potential route to achieving a ten-fold increase in energy storage density over sensible or latent heat thermal energy storage methods [1].

Thermochemical energy storage of high temperature thermal energy features a solar endothermic decomposition reaction followed by an exothermic formation reaction. An important characteristic is that the reaction can go forward or backward within a reasonable temperature range attainable by solar thermal energy. Candidate species for decomposition include oxides, hydrides, hydrates, sulfates, and carbonates [2]. Considerable work has also been carried out on ammonia dissociation [3] and sulfur disproportionation followed by combustion [4].

Perhaps the most elegant design of a TCES subsystem to date is the coupling of high and low temperature metal hydrides. Harries et al. [5] introduced a pathway where H_2 is released from thermal decomposition of a high temperature metal hydride such as CaH_2 and stored in a hydrogen reservoir of low temperature metal hydrides until equilibrium is reached. More recently, $NaMgH_2F$ has demonstrated 1416 kJ/kg of practical energy storage at a decomposition temperature of 478°C. A technoeconomic analysis revealed that the overwhelming cost-driver for this technology is the low temperature metal hydride [6].

Carbonates are especially attractive because of their low cost and high global abundance. Carbonation/decomposition cycling using $CaCO_3$/CaO has been heavily explored for both energy storage [7-13] and carbon capture purposes [14-28]. The drawback to CaO/$CaCO_3$ is the decrease in reactivity during the carbonation reaction, as the capacity for CaO to take up CO_2 is significantly diminished over multiple cycles to roughly one third of the theoretical value [2]. Compounds such as $CaCO_3$ and $BaCO_3$ have been investigated for both energy storage and carbon capture/release applications; however both compounds show loss of reactivity over cycling, which is not acceptable for robust integration with a CSP plant [13, 18, 27, 29].

Use of $SrCO_3$ for energy storage has been previously introduced by Wolfgang and Wasserscheid in 2010 [30]. The scheme is based on the cyclical carbonation/de-carbonation of a SrO/$SrCO_3$ system:

$$SrCO_3 \leftrightarrow SrO + CO_2 \qquad \Delta H^\circ_{rxn,\,25^\circ C} = 234 \text{ kJ/mol}$$

During the solar driven, endothermic step, $SrCO_3$ is decomposed, releasing CO_2 to storage. During times of power generation, CO_2 is then released from storage back to the high temperature receiver/reactor where the reverse, exothermic reaction takes place and heat is transferred to a power block. The high, yet attainable decomposition temperature (ΔG° = 0 kJ/mol at 1175°C) at which the system reaches chemical equilibrium bodes well for generating high temperature thermal energy upon carbonation of SrO — a quality that is lacking in most proposed TCES subsystems.

This project will investigate the ability for a strontium carbonate/strontium oxide based material to facilitate repeatable thermochemical energy storage at a performance level sufficient to meet the SunShot goals. Activities to be performed include a longevity demonstration, kinetic studies, modeling, process design, and development of a technology transfer package for future development.

Introduction:

The main objectives of the project in Year 1 include development of a material processing a demonstrated energy density of at least 4050 MJ/m^3, a peak heat flow of at least 4.0 MW/m^3 and 95% retention of these values over 2000 cycles; using kinetic expressions obtained from fitting the data obtained, the ability to model the reversible reaction on the pore level should be achieved; a process flowsheet shows an exergetic efficiency of the TCES subsystem of ≥ 90% to be attainable; and maximum carbonation and decomposition rates (at their respective optimal temperatures) are greater than those of a $CaO/CaCO_3$ system.

Work Planned for this Quarter**:**

Task 1.1. Longevity tests will be carried out to assess the ability of $SrCO_3$ reactive structures to resist sintering. Thermogravimetric analysis (TGA) cycling studies will be supplemented by solid state characterization techniques such as SEM and BET to determine the effect of cycling on porosity and surface area. If needed, appropriate sintering inhibition techniques will be employed to combat loss of reactivity.

- **Subtask 1.1.1**: Using TGA, evaluate the reactivity of an SPF-G bed for over 500 cycles operation by measuring the mass change over time during temperature swing.
- **Subtask 1.1.2**: Evaluate the porosity (void fraction, pore size distribution, particle size distribution) and surface area of the SPF-G bed before/after 500 cycles via SEM and BET.
- **Subtask 1.1.3**: Based on results of Subtask 1.1.1 in response to the milestone, we will decide to proceed with a 2000 cycle test, fine-tune the SPF-G process, or pursue new synthesis techniques and compare.
- **Subtask 1.1.4**: Using structure decided upon in Subtask 1.1.2, carry out 2000 cycle test via TGA and evaluate original/final porosity and surface area via SEM and BET.
- **Milestone 1.1.1**: Material demonstrates an average volumetric energy density of ≥ 4050 MJ/m3 over cycles 50-2000.
- **Milestone 1.1.2**: The average mass change for cycles 1950-2000 is ≥ 95% of the value for cycles 50-100.
- **Milestone 1.1.3**: Average peak heat flow on a volumetric basis is at least ≥ 4.0 MW/m3 for cycles 50-2000.
- **Milestone 1.1.4**: The average peak rate of mass change for Cycles 1950-2000 is ≥ 95% of the value for Cycles 50-100.
- **Milestone 1.1.5**: Ratio of volumetric energy storage capacity of the $SrO/SrCO_3$ system to that of $CaO/CaCO_3$ is ≥ 1.

Task 1.2. A series of carefully designed experiments will be carried out to determine the kinetic parameters associated with both the surface reaction of a dense pellet and the reaction in a porous sample.

- **Subtask 1.2.1**: Perform isothermal reactions using TGA at several temperatures to ascertain the temperature dependence of the carbonation reaction.
- **Subtask 1.2.2**: Perform an isothermal study using TGA at several partial pressures of CO_2 to determine the dependence of the carbonation reaction on partial pressure of CO_2.
- **Subtask 1.2.3**: Develop a kinetic model incorporating appropriate rate law. Arrhenius parameters will be fit using a non-linear method, with uncertainty determined. The effect of morphological differences between dense pellet and SPF-G samples will also be accounted for.
- **Milestone 1.2.1**: Arrhenius parameters determined to within a 5 % uncertainty. Goodness-of-fit tests will be used to fit the model to the data and determine the uncertainty.
- **Milestone 1.2.2**: The rate of SrO carbonation is greater than that of CaO carbonation at their respective optimum temperature at atmospheric pressure.

Task 1.3. A combination of conventional TGA and Solar TGA studies to obtain kinetic data for the decomposition reaction under a variety of conditions will be performed.

- **Subtask 1.3.1**: Perform decomposition experiments using Solar TGA to acquire initial rate data at several different temperatures.
- **Subtask 1.3.2**: TGA studies of $SrCO_3$ at several decomposition temperatures with replication to produce data showing the progression of reaction extent versus time. Sensitivity to the partial pressure of CO_2 will also be studied.
- **Subtask 1.3.3**: Kinetic modeling of both conventional and Solar TGA results to determine the solid state kinetic model. A non-linear fitting scheme will perform minimization of a least-squares objective function.
- **Milestone 1.3.1**: Arrhenius parameters determined to within a 5 % uncertainty. Goodness-of-fit tests will be used to fit the model to the data and determine the uncertainty.
- **Milestone 1.3.2**: Ratio of peak rates at respective optimum temperatures for decomposition of $SrCO_3$ and $CaCO_3$ is ≥ 1.

Task 1.4. Develop a direct pore-level model for fluid flow, heat transfer, and chemical reaction inside porous $SrO/SrCO_3$ structure based on 3-dimentional (3D) real geometry obtained from micro-scale Computer Tomography (CT) in solid and fluid phases.

- **Subtask 1.4.1**: Obtain tomography images for porous $SrO/SrCO_3$ structures at initial stage and after multiple cycles; segmentation and image processing to render representative 3D structures of samples.
- **Subtask 1.4.2**: Simulate the fluid flow inside the porous structure in a range of typical Reynolds numbers to obtain the permeability and Forchheimer constant.
- **Subtask 1.4.3**: Simulate the heat transfer including conduction, convection and radiation in porous media to obtain the effective heat transfer coefficient and thermal conductivity.

- **Subtask 1.4.4**: Validate the simulated transport properties with available data in the literature and experimental measurements.
- **Subtask 1.4.5**: Simulate the transient chemical reaction coupled with fluid flow in the 3D structures of different porosities to determine the optimal structure that is able to produce the highest volumetric heat flow rate.
- **Milestone 1.4.1**: The computed transport properties including permeability and effective thermal conductivity of porous $SrO/SrCO_3$ structure from direct pore-level simulation at high temperatures are compared with theoretical bounds, empirical models, and experimental measurements. The relative difference from experimental findings is demonstrated to be < 20%.
- **Milestone 1.4.2**: Heat flow rates computed from pore-level simulation of the chemical reaction rate for different porous structures will be reported. The average volumetric heat flow rate for an optimized structure is ≥ 4.0 MW/m^3.

Task 1.5. Using input from both the literature and prior milestones, a system-level analysis will be performed to determine overall $SrO/SrCO_3$ system process viability. A process flowsheet will be used to quantify the energetic and exergetic efficiency, as well as the time required to store CO_2. Of specific interest is the matching of the rates of various sub-processes (heat transfer, chemical kinetics, absorption, etc).

- **Subtask 1.5.1**: Create process flowsheets for different configurations based on existing process flow diagram.
- **Subtask 1.5.2**: Using process flowsheets, carry out a probabilistic analysis of overall exergetic efficiency to the variation of process parameters (e.g. CO_2 storage rate and compression ratio).
- **Milestone 1.5.1**: The process model must demonstrate an upper bound overall exergetic efficiency, η_{ex}, of at least 90% for the TCES subsystem.
- **Milestone 1.5.2**: The kinetics of the carbonation reaction and CO_2 storage release allow for a peak rate of heat generation from the bed that matches 95% of the likely peak heat flow rates as determined in Milestone 1.4.2.

Task 1.6: The technology to market transition will begin with formulation of a summary business plan. This plan will include: business model, summary financial model and capitalization strategy, the logical first market entry, potential strategic partners, product roadmap and key strategic milestones from which technology transfer and outreach can occur.

- **Subtask 1.6.1**: Develop licensing option with UF for intellectual property associated with the project.
- **Subtask 1.6.2**: Develop “Pitch” presentation for partners and to launch technology into market.
- **Subtask 1.6.3**: Attend at least one business-technical conference to introduce the concept on a non-confidential basis.
- **Subtask 1.6.4**: Based on interest, compile list of potential strategic partners or potential sources of follow-on funding.

- **Milestone 1.6.1**: Summary Business Plan complete, List of 6-10 potential strategic partners for future product development and go to market support. Summary business plan will include a sensitivity analysis to identify the 3 greatest cost drivers for proposed technology with a comparison to existing literature on $CaO/CaCO_3$ technologies.
- **Milestone 1.6.2**: Demonstrable investment of time or money in our technology from an outside entity.

Project Results and Discussion:

Task 1.1: Longevity tests will be carried out to assess the ability of $SrCO_3$ reactive structures to resist sintering. Thermogravimetric analysis (TGA) cycling studies will be supplemented by solid state characterization techniques such as SEM and BET to determine the effect of cycling on porosity and surface area. If needed, appropriate sintering inhibition techniques will be employed to combat loss of reactivity.

Subtask 1.1.1: Using TGA, evaluate the reactivity of an SPF-G bed for over 500 cycles operation by measuring the mass change over time during temperature swing.

TGA screening results reported in Q2 for $SrO/SrCO_3$ structures prepared with SPF-G show that for most samples the energy density degraded to the level < 1500 MJ/m^3 after 5 cycles. Extended TGA testing for 15 cycles showed continuous decrease in energy density possibly due to particle sintering. In this quarter, sintering inhibitor is further explored and a screening TGA experiment has been conducted to identify the most suitable candidate.

Various conventional materials including silica, alumina, zirconia, YSZ (yttria stabilized zirconia), and titania are used as supporting material to avoid sintering of reactive particles in thermochemical processes. Our earlier experiments confirmed that SrO reacts with these materials to form mixed oxides including strontium silicate, strontium aluminate, strontium zirconate, and strontium titanate, via solid state chemical reactions. This phenomenon adversely affects the performance of the systems in terms of energy storage capacity. To overcome this challenge, a new class of materials is introduced that can serve as supporting material. It is proposed that mixed oxides composed of strontium oxide and conventional supporting materials (silica, alumina, YSZ etc.) are likely to exhibit inert behavior towards reactive substrate and are probable candidates as a supporting material for $SrO/SrCO_3$ based TCES.

Amongst the conventional materials used as a supporting material, yttria stabilized zirconia (YSZ) is highly stable at higher temperature, thus a YSZ/SrO material is investigated as a prime candidate among other materials (strontium zirconate synthesized using YSZ will henceforth be referred SrYSZ).

Given the long term stability issues seen with tested SrO-based samples, the inclusion of barium oxide (BaO), as well as BaO alone, was also investigated. In an effort to find a more productive high temperature chemistry, it was hypothesized that barium carbonate may be a more promising candidate by virtue of its higher decomposition temperature at atmospheric pressure.

Material synthesis

Strontium zirconate (supporting material):

Strontium oxide (Alfa Aesar) and 8mol% YSZ (99.9%, Advanced Materials) were taken as received in powder form and mixed in 1:1 molar ratio. The mixture was heat-treated in a muffle furnace at 1500 ^oC for 8 hours under air. During this process, strontium zirconate is synthesized via solid state reaction between strontium oxide and YSZ. XRD analysis of the sample confirms formation of the strontium zirconate ($SrZrO_3$) (See Figure

1). Strontium zirconate is stable under operating conditions observed for $SrO/SrCO_3$ looping cycle and can be used as a supporting material to inhibit sintering of reactive particles and retain the active surface area. Powder of strontium zirconate was sieved to prepare samples in different size ranges for screening purposes: 25-38μm, 38-63μm, 63-106μm, and 106-125μm.

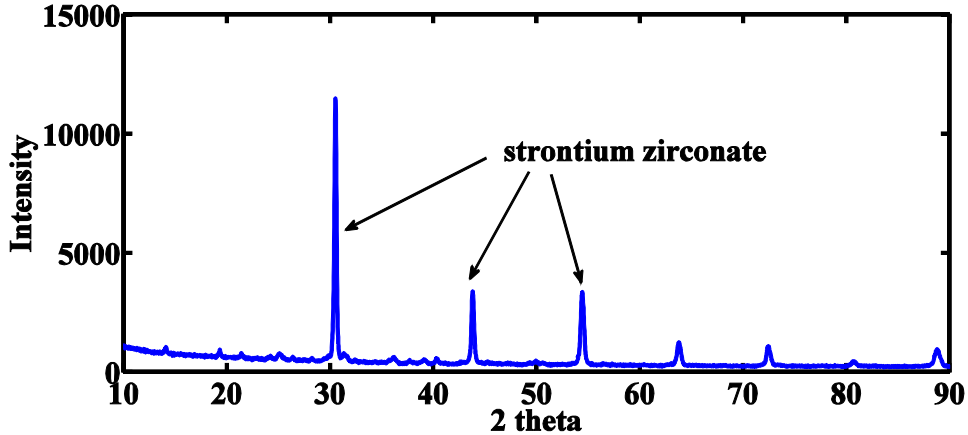

Figure 1: XRD plot of strontium zirconate sample synthesized by solid state reaction of SrO and YSZ.

Strontium oxide (reactive material)

Strontium oxide (Alfa Aesar) was taken as received in powder form and heat treated at 1500°C under air. Heat treated strontium oxide is sieved and samples with different particle size ranges including, 25-38μm, 38-63μm, 63-106μm, and 106-125μm, were prepared. Strontium oxide is highly hygroscopic in nature and likely to absorb moisture from air to form hydrates of strontium ($Sr(OH)_2$, $Sr(OH)_2.8H_2O$)). Thus, the reactive material was likely a mixture of strontium oxide, strontium hydroxide monohydrate and strontium hydroxide octa-hydrate.

Mass ratio of supporting material to reactive material:

The mass ratio of reactive material to supporting material must be optimized to: a) inhibit sintering of the reactive particles, and b) maximize the mass of reactive material to achieve higher energy density. For the baseline case it is proposed that, for every reactive particle, one particle of supporting material must be available in the reactive structure to provide adequate buffer between two reactive particles. It is acknowledged that, for the mixture of powder samples, number of particles of the constituent in the mixture, and not their mass, is critical parameter that determines the stability of the reactive system. Figure 2 shows the schematic of ideal distribution of particles in the structure.

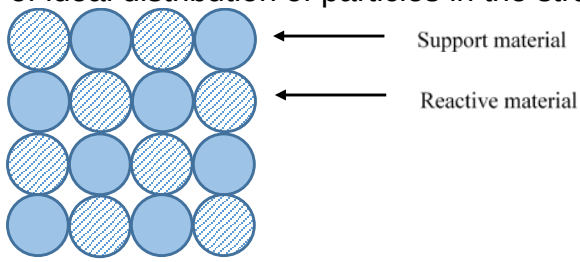

Figure 2: Schematic of an ideal distribution of particles of reactive material and supporting material in the reactive structure.

This hypothesis is used as a basis to estimate the mass ratio of supporting material to reactive material. The main assumptions include that all the particles have a spherical shape, and the particles themselves do not have any porosity. In addition, it was assumed that density of $Sr(OH)_2$ represents average density of mixture of SrO, $Sr(OH)_2$, and $Sr(OH)_2.8H_2O$. For the baseline case (with the same particle sizes and the same number of particles), the mass ratio, γ, is thus

$$\gamma = \frac{M_R}{M_S} = \frac{\rho_R}{\rho_S} = \frac{3.62 g/m^3}{5.46 g/m^3} = 0.66$$

where ρ_R and ρ_S are the densities of the reactive strontium hydroxide and the supporting strontium zirconate, respectively. The mathematical analysis indicates that, the mass of reactive material should be 0.66 times the mass of supporting material if they have the same size.

Barium oxide (reactive material)

SrO was combined with barium oxide in an attempt to port some of BaO's apparently greater degree of stability. Samples were prepared with 40% SrO and 60% BaO. Barium oxide prepared by decomposition of barium nitrate at 1000°C for 4 hours was ball milled with strontium oxide for 2 hours. The mixture was then heat treated in a muffle furnace at 1500°C for 8 hours. Two samples were prepared: the first is an unstructured powder prepared by crushing the heat treated mixture to a particle size range of 25μm – 38 μm while the second is formed with the SPF-G method for which the heat treated mixture was ground to very fine powder. Thus, the second powder sample is mixed with graphite and sintered into a porous structure before cycling begins. In this case, nano-sized graphite powder was mixed in a 4:1 sample-to-graphite ratio. Sintering is conducted in the TG at 1100°C for three hours and the carbon is burned out with O2 for one hour at 1000°C immediately prior to cycling. To calculate the energy density, both the ΔH of SrO (234 kJ/mol at 25°C) and the ΔH of BaO (272 kJ/mol at 25°C) were considered. Given the composition of the samples, a weighted average of 256.8 kJ/mol was used to calculate energy density.

TGA Procedure

Samples were subjected to three hours of carbonation at 1150°C under 120 sccm of CO_2 and thirty minutes of decomposition at 1235°C under 90 sccm of argon and 10 sccm of CO_2. This environment of 10% CO2 during decomposition is used to more accurately simulate a real system which is unlikely to operate in a pure inert environment. Prior to cycling, however, samples are heated at 1100°C for three hours to remove moisture that has been absorbed by SrO during preparation, transportation, and storage. Mass loss of samples came to equilibrium during each experiment during the step, implying a sufficient removal of moisture so that TGA data during cycling is more accurate. For screening purposes, each sample is subjected to 5-15 cycles. Figure 3 depicts representative TGA data of one such 15-cycle experiment. After experimentation, the sintered structure is weighed and then carefully measured with a vernier caliper so its volume can be recorded. To counter moisturization and prepare for imaging, samples are finally suspended in epoxy.

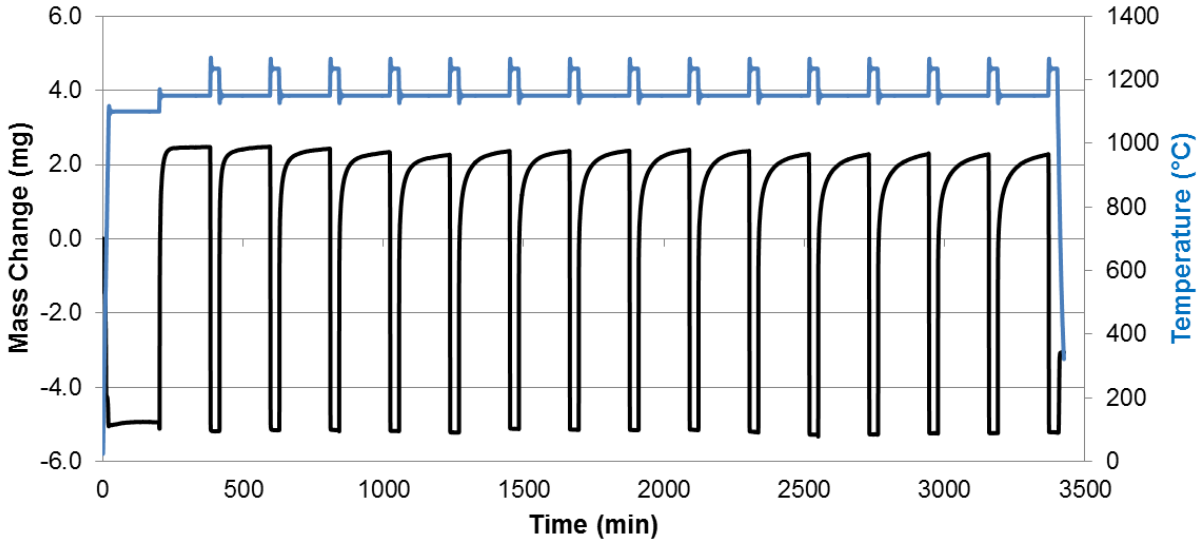

Figure 3: TGA data of 15-cycle screening experiment with a 32% (by mass) SrO in SrYSZ mixture with particle sizes of 38-63 µm.

TGA Results

Each tested sample is initially a mixture of strontium hydroxide and an inert supporting material. The initial TGA step rids the sample of moisture and results in a mixture of strontium oxide and supporting material. The mass loss observed during the demoisturization step is subtracted from the initial sample weight and is used to determine the real strontium oxide content (by mass) of the mixture. The result is a tight range of SrO content across all samples depending on their original intended strontium hydroxide content.

Energy density for each cycle is determined using a sample's final mass, measured volume, the mass change observed during the cycle, and the heat of reaction for the strontium carbonate system: 234 kJ/mole at 25°C. The peak power density is also calculated using the TGA's DTG function which measures the rate of rate change of mass change.

The cyclic energy densities for a summary of selected samples tested in screening experiments are presented in Figure 4 and Figure 5. The respective sample descriptions are detailed in Table 1 and Table 2. Figure 4 shows results for strontium oxide mixed with different variations of the inert SrYSZ supporting material while Figure 5 shows results for SrO mixed with $SrZrO_3$ (commercial) and other supporting materials. During screening, SrO supported with either SrYSZ or $SrZrO_3$ was seen to surpass performance from SrO mixed with other supporting materials: MgO, $SrTiO_3$, and $SrAl_2O_4$. Thus, screening experiments focused on comparing and optimizing those supporting materials. Factors that were altered to find the best combination were particle size and the ratio of SrO to supporting material.

Three particle size ranges were tested: 25-38 µm, 38-63 µm, and 63-106 µm. The range 38-63 µm served as our baseline particle size, and most samples contain that range. Smaller particle sizes may provide more surface area for reaction but they are also more susceptible to sintering. For the SrYSZ supporting material, Samples A and B are identical apart from the smaller particle size of B. The performance of Sample A is greater than that of Sample B for each of the 15 cycles. Likewise, when comparing Samples D

and E one can see that Sample D (38-63 µm) outperforms Sample E (63-106 µm). For the purposes of screening SrYSZ samples, 38-63 µm appears to be the best particle size range tested. The case of $SrZrO_3$ samples showed different results. Sample F (25-38 µm) initially outperforms Sample G (38-63 µm) but later appear to achieve similar equilibrium points.

Samples with lower SrO content, such as D, E, and H, exhibited greater stability than those with larger shares of SrO. There is a trend of increased initial energy density during the first cycle with increased SrO content, however. Such results imply that larger shares of supporting material inhibit the sintering of SrO over 15 cycles and result in less variation of energy density from one cycle to the next. Samples with more SrO content, such as A, B, C, F, and G appear to be more susceptible to sintering of reactive SrO, incurring effective surface area loss along with loss of energy density. While production decreases from its initial value for those samples with greater SrO content, many of them still show greater energy density by their 15th cycles than samples with less SrO. Additionally, most of the samples appear to be reaching an asymptotic equilibrium point. There should be an SrO content at which an optimal combination of stability and energy density equilibrium exists. Sample C, which contains over 50% of real SrO content, reaches an equilibrium of cyclic energy density below that of all other SrYSZ samples. This implies that the optimal SrO content may lie in the range of 40-50%.

The two supporting materials with which strontium oxide has exhibited the greatest energy density over fifteen cycles are SrYSZ and $SrZrO_3$. Each tested sample with $SrZrO_3$ in Table 2 has an analogy with SrYSZ in Table 1. Samples B and F, containing ~45% SrO and 25-38 µm particle sizes, performed similarly over fifteen cycles and appear to need additional cycles to reach a point of equilibrium. Samples D and H each show stability over fifteen cycles, but Sample D with YSZ exhibits greater energy density even with a less SrO content. Similarly, Sample A outperforms Sample G even though the $SrZrO_3$–supported Sample G contains more reactive strontium oxide. In each case, the sample with SrYSZ performed similarly or outperformed the associated sample with $SrZrO_3$. These results lead to the initial conclusion that SrYSZ may act as a superior supporting material to $SrZrO_3$ under these conditions.

Table 1: Identification of SrO + SrYSZ samples tested in screening experiments.

Label	Supporting Material	Labeled SrO Content	Real SrO Content	Particle Size (µm)
A	SrYSZ	50%	50.6%	38-63
B	SrYSZ	50%	44.0%	25-38
C	SrYSZ	60%	52.7%	38-63
D	SrYSZ	40%	43.2%	38-63
E	SrYSZ	40%	39.7%	63-106

Table 2: Identification of mixtures of SrO + $SrZrO_3$ and other supports tested in screening experiments.

Label	Supporting Material	Labeled SrO Content	Real SrO Content	Particle Size (µm)
F	$SrZrO_3$	50%	46.9%	25-38
G	$SrZrO_3$	50%	48.3%	38-63
H	$SrZrO_3$	40%	37.9%	38-63
I	MgO	40%	34.3%	38-63
J	$SrTiO_3$	40%	37.6%	38-63
K	$SrAl_2O_4$	40%	37.7%	38-63

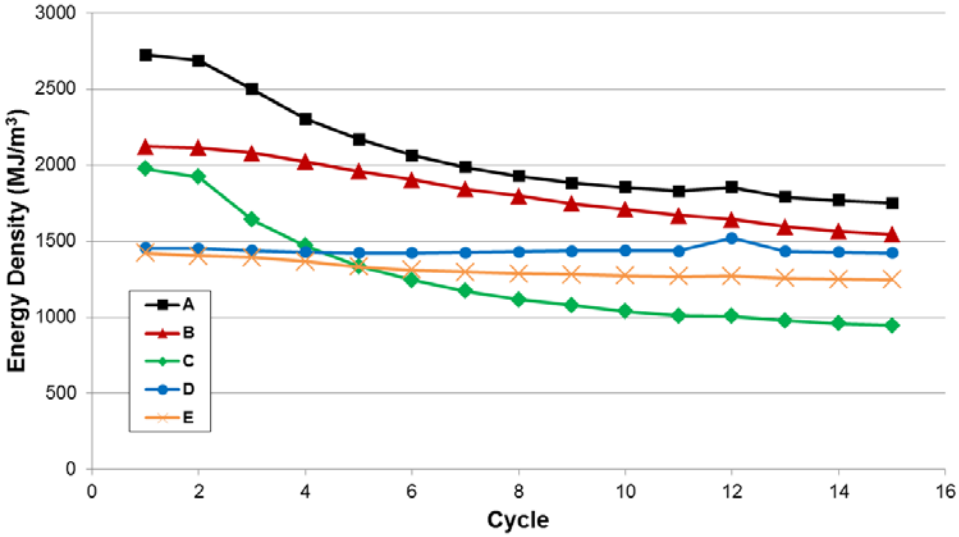

Figure 4: Calculated cyclic energy density from screening experiments for SrO + SrYSZ samples.

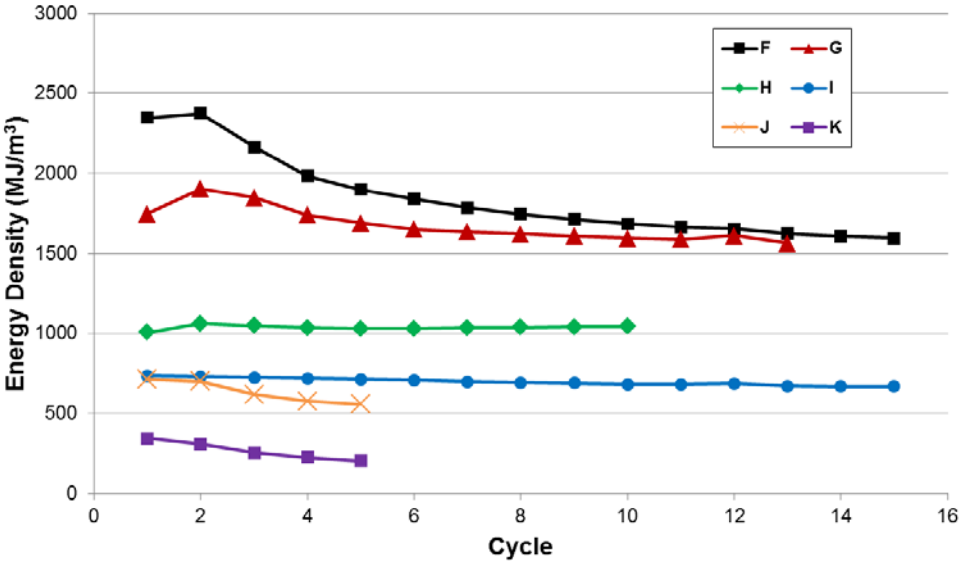

Figure 5: Calculated cyclic energy density from screening experiments for samples containing mixtures of SrO with $SrZrO_3$ and other supports.

The overall comparison amongst Samples A to K shows that D is the most stable reactive sample and delivers a high energy density of 1450 MJ/m^3 over 15 consecutive cycles. For sample D (γ=0.66), the number of reactive and supporting particles are identical and is likely reason for its highly stable performance. Sample A showed the highest initial peak energy density of 2722 MJ/m^3 but it progressively decreases with consecutive cycles till 1750 MJ/m^3 after 15 cycles. For sample A (γ=1), the number of reactive particles is more than supporting particles. Thus there exists unsupported reactive particles that might have sintered during each cycle causing loss of surface area and a corresponding decrease in energy density. This comparison shows that, to increase the energy density without compromising the stability of the reactive structure, SrO content in the sample should be increased while there should be enough supporting particles to prevent sintering. This leads to the idea of using supporting particles of smaller size. TGA screening experiment is underway and more results will be report in the next report.

The peak power density of each cycle was calculated for each sample. This data is shown in Figure 6. Average peak power density appears to follow energy density. Samples A, B, and F lead in both energy density and peak power density. Each sample, with the exception of K, surpasses the SOPO milestone of 4 MW/m^3.

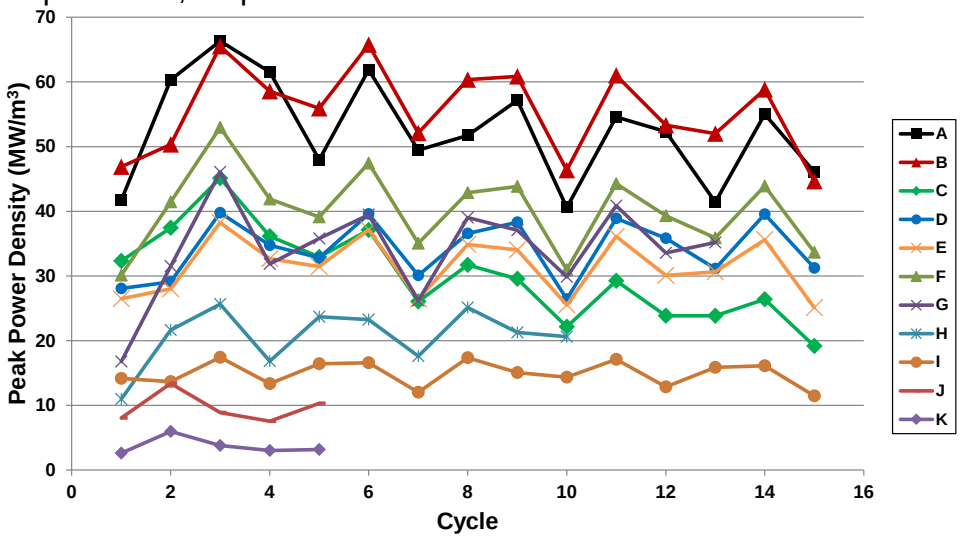

Figure 6: Peak power density for each cycle of each sample.

The sample that shows the greatest energy density over 15 cycles is Sample A: SrO + SrYSZ with approximately 41% SrO content and 38-63 µm particle sizes. To verify its repeatability, two additional identical experiments were run. Results for these runs have been averaged in Figure 7.

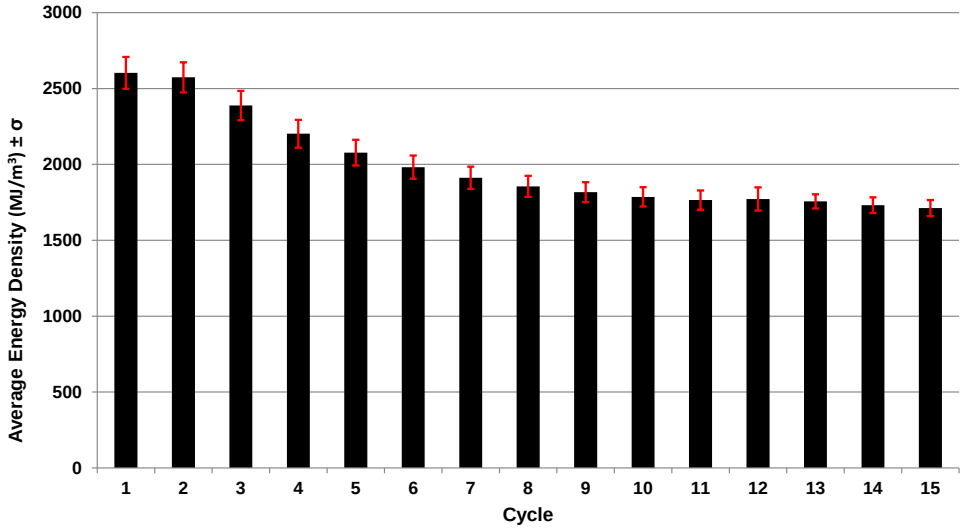

Figure 7: Average energy density with standard deviation for three experiments of Sample A over fifteen cycles.

The average peak energy density is approximately 2600 MJ/m^3 while that at the fifteenth cycle is approximately 1700 MJ/m^3. Additionally, standard deviation decreases with increasing cycle number, ranging from 4.0% for Cycle 1 to 3.1% for Cycle 15.

Figure 8 shows TG data of mass change of pure barium oxide (25-38 µm) over 10 cycles with 3 hour carbonation steps at 1150°C under 100% CO2 and 1.5 hour decomposition steps at 1235ºC with 10% CO2. Barium oxide displays promising stability over 10 cycles at an energy density of approximately 1420 MJ/m^3.

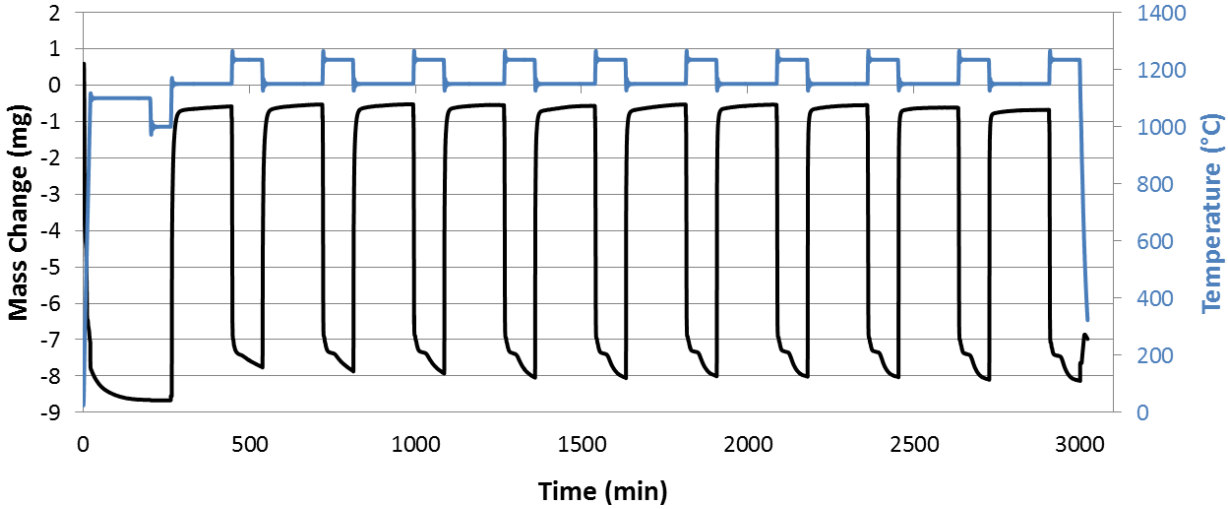

Figure 8: TG mass change data of 10 cycles of barium oxide powder (25-38 µm).

Figure 9 shows the TG mass change profiles for 10 cycles between 1150°C and 1235°C of the first 40% SrO with BaO unstructured powder sample. Full carbonation appears to be achieved for each cycle, resulting in good stability over 10 cycles. The average energy density over these cycles is approximately 1344 MJ/m^3. Features of both SrO and BaO are evidenced in the profiles seen in Figure 9. The first cycle achieves full carbonation very quickly, a feature of the carbonation of BaO (as seen in each cycle of Figure 8). However, by the 10th cycle, carbonation kinetics have slowed. This can be inferred from the greater time to reach full carbonation in the last cycle and the more "rounded" shape of its profile. This behavior is seen in similarly prepared SrO samples, but to a greater degree. Thus, it is possible that a SrO/BaO mixture may display greater stability than a pure SrO sample.

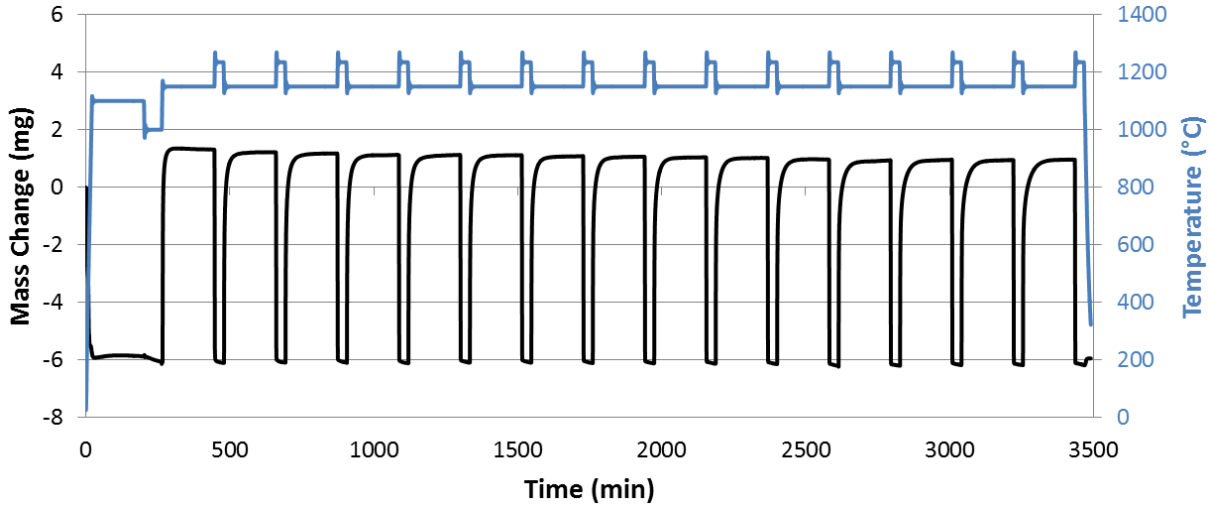

Figure 9: TG mass change data of 10 cycles of 40% SrO and 60% BaO powder.

The mass change for the structured SPF-G sample prepared with 20% nano graphite is shown in Figure 10. Like other samples with BaO, an impressive degree of stability is noted through a limited number of cycles. Energy density is approximately 1030 MJ/m^3 for the SPF-G sample, nearly 24% less than that of the unstructured powder. The SPF-G sample also seemingly demonstrates more consistent kinetics than the unstructured powder sample, as carbonation profiles appear relatively constant. This is only an abbreviated test, however, and further cycling is needed to confirm the behavior. It should further be noted that the flat carbonation profiles prior to reaching the full reaction extent could be evidence of slow diffusion. A future hypothesis to test could be that higher carbonation temperatures will hasten the carbonation and thus increase the practical carbonation conversion over reasonable timeframes (e.g. hours). This temperature dependence has been noted in the SrO carbonation studies.

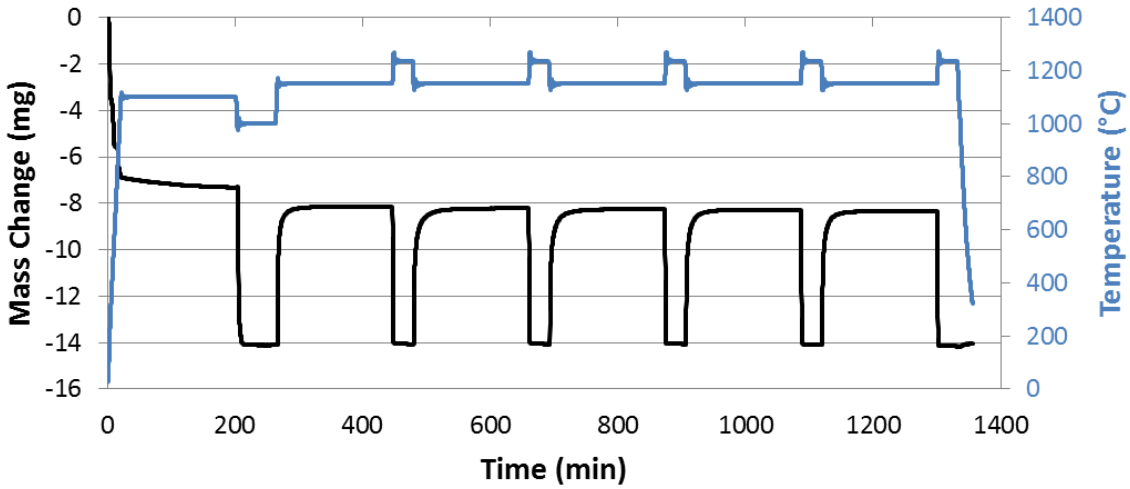

Figure 10: TG mass change data of 5 cycles of 40% SrO and 60% BaO SPF-G sample.

Subtask 1.1.2: Evaluate the porosity (void fraction, pore size distribution, particle size distribution) and surface area of the SPF-G bed before/after 500 cycles via SEM and BET.

Samples for SEM imaging were prepared by placing a piece of the porous structure in a plastic mold which was then filled with epoxy. The hardened sampled was then polished and coated with a conductive Au-Pd coating. The model of SEM that was primarily used for this work was the JEOL SEM-6400, which uses a tungsten filament and has a standard electro-magnetic lens system. The system has a resolution of up to 3.5 nm and a magnification capability of up to 300000 times. A working distance of 15 mm and a beam acceleration of 15 KV was used.

The SEM images for Sample B (particle size 25-38 µm before cycling) in Table 1 at different magnifications are presented in Figure 11 (a-c).

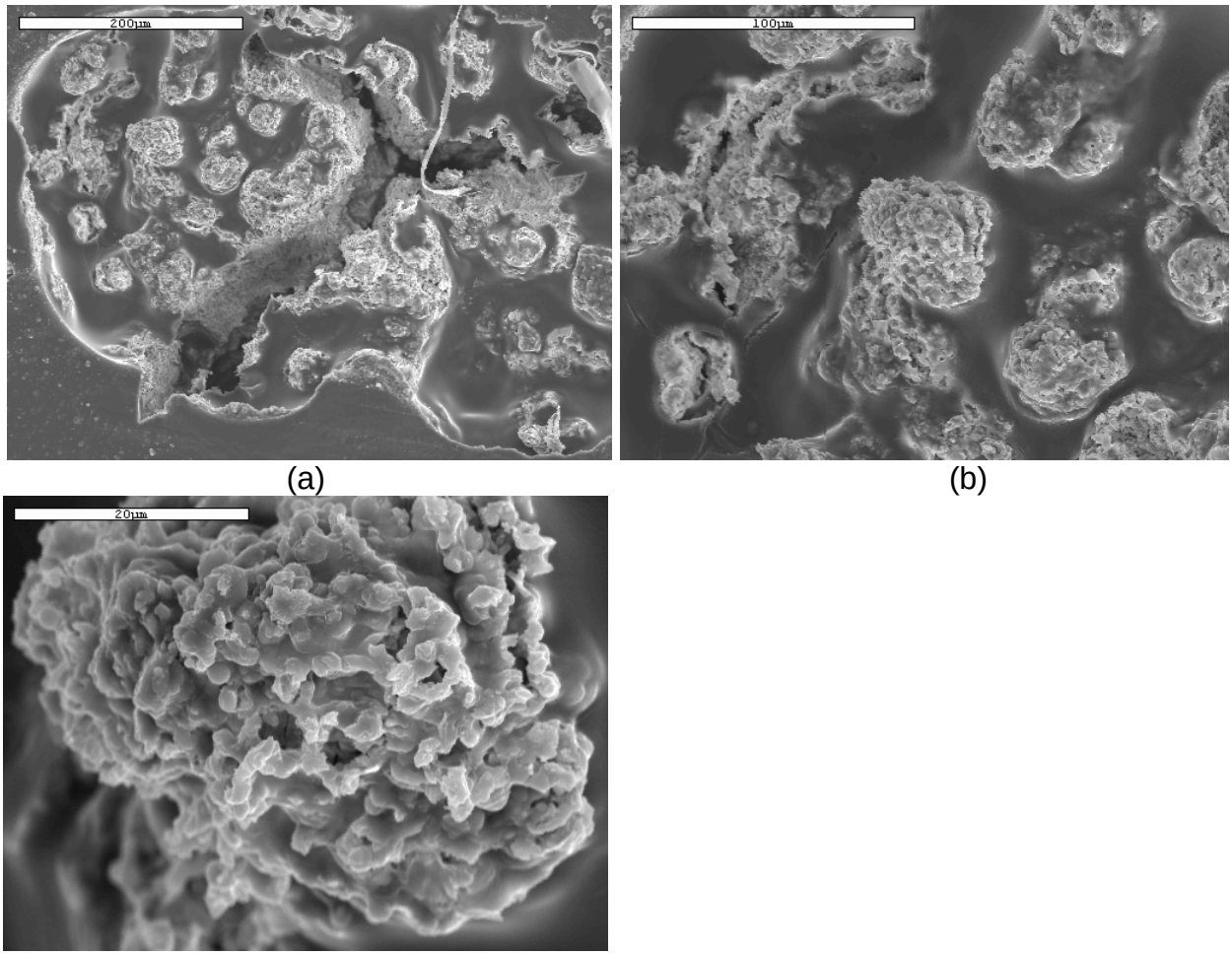

(a) (b) (c)

Figure 11: SEM image of Sample B in Table 1 at (a) 250x magnification, (b) 500x magnification, and (c) 2500x magnification.

Figure 11 (a, b) shows that the sample maintains a good porosity even after 15 cycles. It is also noticed in Figure 11 (c) that there are micropores (a few microns) on the surface of a single particle.

Structure porosity and surface area characterization via BET will be conducted for different samples once the Nova 1200 porosimeter at UF is functional. It has been under repair for several weeks.

Subtask 1.1.3: Based on results of Subtask 1.1.1 in response to the milestone, we will decide to proceed with a 2000 cycle test, fine-tune the SPF-G process, or pursue new synthesis techniques and compare.

For a longevity study, a chosen sample will exposed to cycles similar to that of the screening experiments. For logistical purposes, the longevity study will proceed with 1 hr of carbonation and 15 minutes of decomposition. Relative to the screening experiments, some performance will be lost during the 1 hr carbonation steps. However, we estimate that approximately 89% of performance seen during 3 hr carbonation steps is expected during the first hour of carbonation.

Given its best observed performance and repeatability over fifteen cycles in Figure 4 and Figure 5, Sample A in Table 1 (~50 wt.% SrO) in SrYSZ with 38-63 µm particle size for both is chosen for a longevity experiment. The TGA data and energy density for the first 100 cycles are presented in Figure 12 (a, b) respectively.

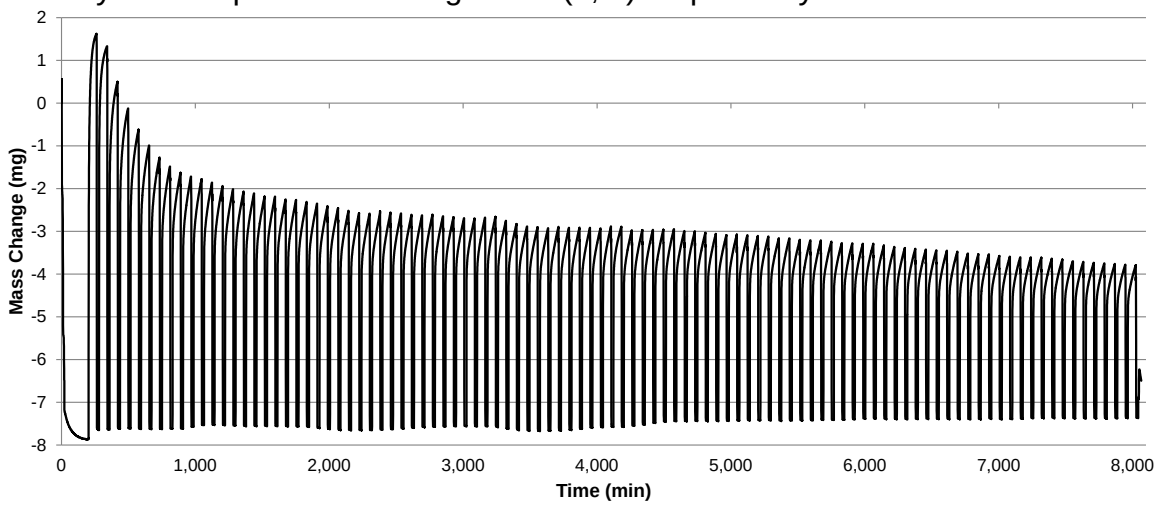

(a)

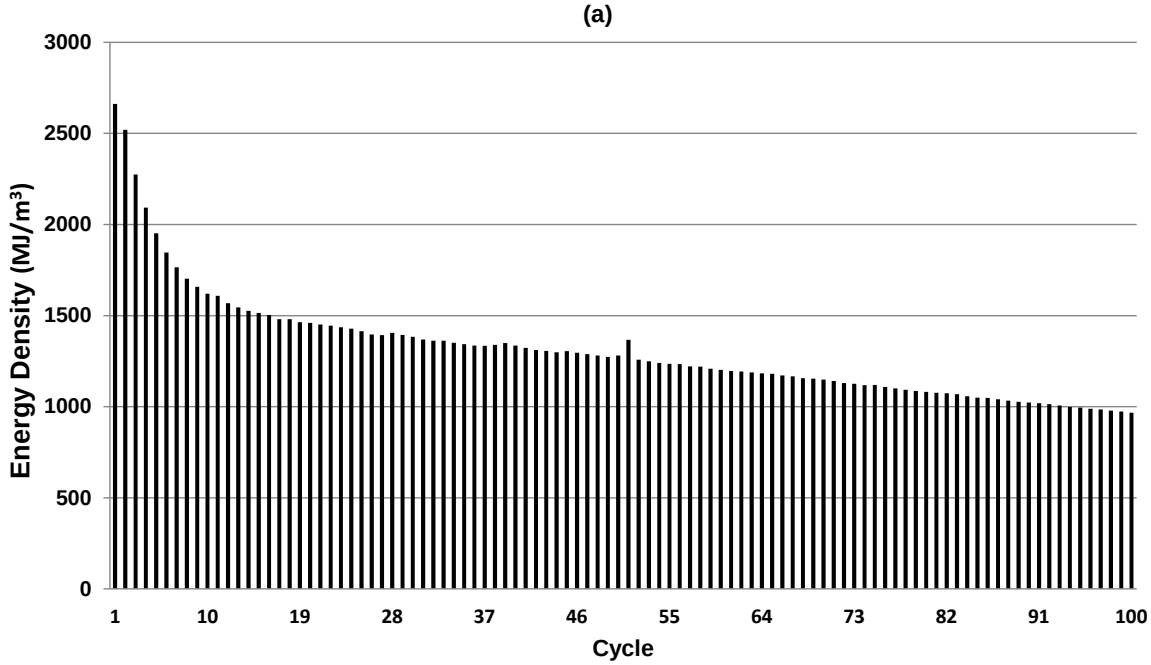

(b)

Figure 12: (a) TGA mass change data, and (b) calculated energy density of 100-cycle for Sample A in Table 1 with 50 wt.% SrO in SrYSZ and 38-63 µm particle size.

The results in Figure 12 show that the performance of Sample A degrades with cycles. After 100 cycles, the energy density drops to about 1000 MJ/m^3. The decrease in performance for this extended cycling can be mitigated by regenerative carbonation at higher temperatures. Figure 14 in Task 1.2 clearly shows that the extent of carbonation is higher at higher temperatures. A similar phenomenon was observed by Valverde et al. [31, 32] who used this as a strategy to improve the capacity of the calcium oxide in their study. The principle of this regenerative method is to develop thermal shocks within the material structure by carbonating at higher temperature followed by sudden calcination. This leads to formation of micro cracks within the particles and increases the specific

surface area of the material. Figure 13 shows the improvement achieved in [31] by recarbonation at higher temperatures before calcination.

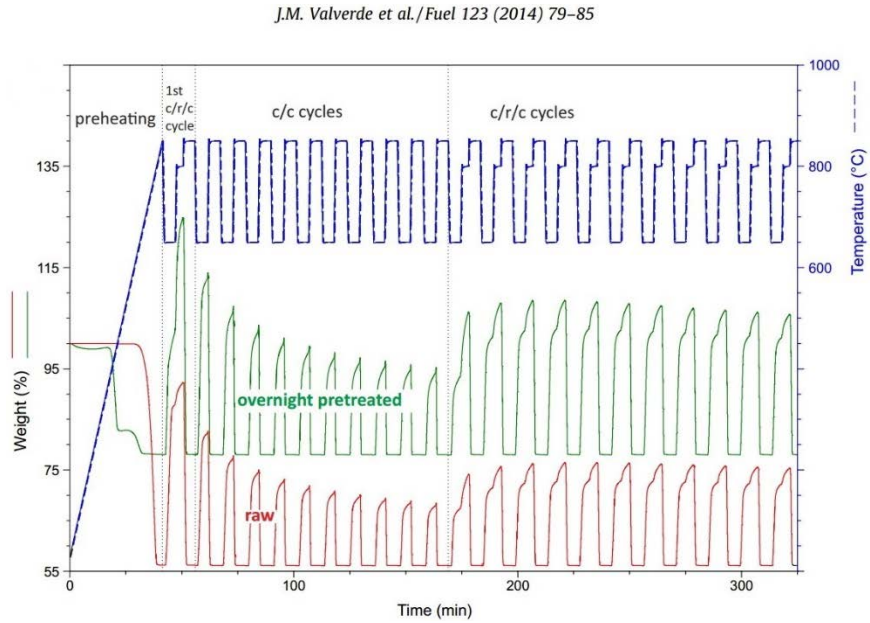

Figure 13: Time evolution of sorbent weight % during the 1st carbonation/recarbonation/calcination cycle followed by 10 carbonation/calcination cycles and 11 carbonation/recarbonation/calcination cycles for heat treated and raw limestones from Valverde et al. [31]

As the strontium oxide has additional SrYSZ material spacers the change in surface area created by the application of this regeneration method is expected to be more prominent due to the difference in thermal expansion coefficients of the materials. This method shall be explored along with the optimization of material parameters of the system and is expected to improve the performance of the $SrO/SrCO_3$ TCES system substantially.

Subtask 1.1.4: Using structure decided upon in Subtask 1.1.2, carry out 2000 cycle test via TGA and evaluate original/final porosity and surface area via SEM and BET.

This subtask will be conducted once the optimal sample components and structure have been determined in Subtask 1.1.3.

Task 1.2: Carbonation Kinetics

Subtask 1.2.1: Perform isothermal reactions using TGA at several temperatures to ascertain the temperature dependence of the carbonation reaction.

In Task 1.1, a 1:1 mass ratio of $SrO/SrZrO_3$ demonstrated excellent productivity over 15 cycles. To study the carbonation kinetics of this leading candidate material, the sample was prepared identically to the procedure used in Task 1.1.

An initial inert purge at 1000°C was used to decompose the sample to a minimum asymptotic mass at which point the sample was assumed to consist of only SrO and $SrZrO_3$. Next, the sample was put through a series of isothermal carbonation/decomposition cycles. Decomposition was performed at 1235°C each cycle under a flow of 100 sccm N_2, after which carbonation was carried out at 900, 1000, 1100, 1150, 1200, 1235 and 1300°C under pure CO_2 (100 sccm). Between steps, temperature was changed at 100°C/min under the same gas environment as the previous step. Once temperature reached the desired setpoint, gas flows were switched to the gas of interest to begin the reaction. Random numbers were associated with each temperature and then sorted to determine the trial order and minimize any potential systematic error. Three cycles at each temperature were carried out. Reaction extent (α) and heat flow from the 3rd set of data is shown in Figure 14 and Figure 15, respectively. In calculating the extent, α, it was assumed that $SrZrO_3$ did not take place in carbonation/decomposition, however we speculate that there is some baseline reactivity due to free SrO.

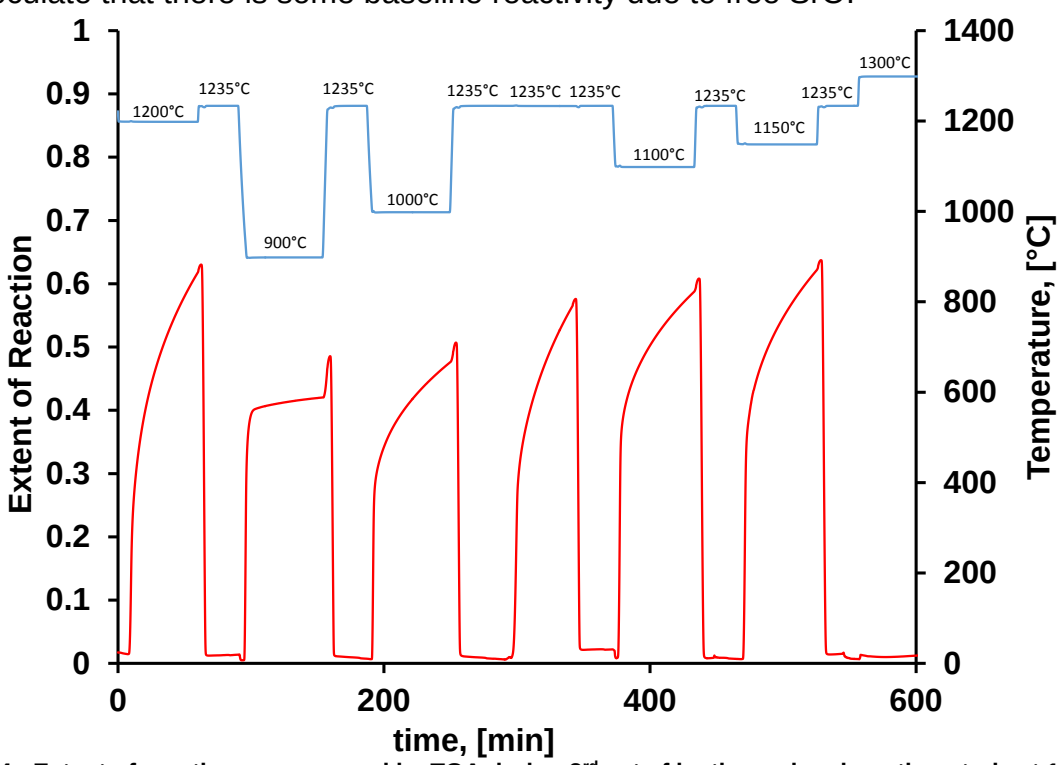

Figure 14: Extent of reaction as measured by TGA during 3rd set of isothermal carbonation study at 1200, 900, 1000, 1235, 1100, 1150, and 1300°C. Decomposition under 100% N_2 was carried out at 1235°C in each case. CO_2 flow was maintained during temperature changes, which resulted in additional carbonation after runs at lower temperatures (e.g. 900°C) as temperature increased.

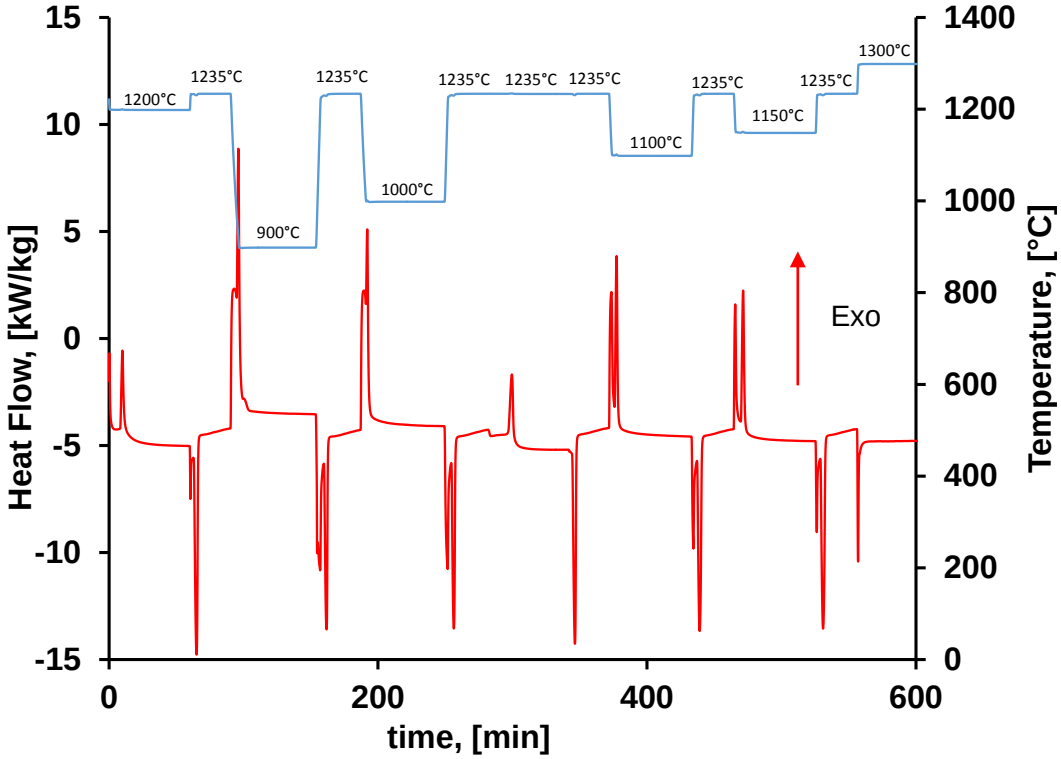

Figure 15: Heat flow from 1:1 SrO:$SrZrO_3$ sample during 3rd set of isothermal temperature experiments.

No appreciable carbonation occurs at 1300°C, which is not surprising considering the temperature is far past the equilibrium temperature (1175°C at 1 atm). Although all samples reached a reaction extent that is within thermodynamic predictions, it is interesting to note that *higher* temperature carbonation resulted in *greater* reaction extent after the given amount of time. Though these observations are in contrast to thermodynamic predictions, they agree well with previous work with CaO carbonation [33, 34]. This is likely due to greater solid phase transport of CO_2 through the $SrCO_3$ product layer at higher temperatures. Though lower temperature carbonation should theoretically have higher final reaction extents, slow diffusion makes this ultimate extent practically unachievable within reasonable time frames.

Figure 15 shows the heat flow in and out of the sample. As expected, carbonation yields an upwards exothermic peak while the opposite occurs for decomposition. More interestingly, an earlier peak is observed during the temperature ramp. In the case of carbonation, CO_2 was not started until the temperature had stabilized at the temperature of interest. A phase transition of $SrZrO_3$ at 1170°C has been reported by de Ligny and Richet el al. [35], while there are also other accounts of $SrCO_3$ phase transitions at temperatures ranging from 900-1100°C [36]. This is of major interest, as it could mean that additional energy is being consumed/released form a solid-solid phase transition that had not been accounted for previously.

In order to avoid confusion between actual kinetic or thermodynamic attributes and material degradation, isothermal experiments were carried out using fresh SrO powder which had been heat treated for 8 hrs at 1500°C, crushed, and sieved to a specified size range. Each experiment utilized a new sample of SrO powder to

eliminate any history effect. In Figure 16, trials at 800 and 900°C show clearly inferior performance, whereas all temperatures 1000°C or greater show comparable extents.

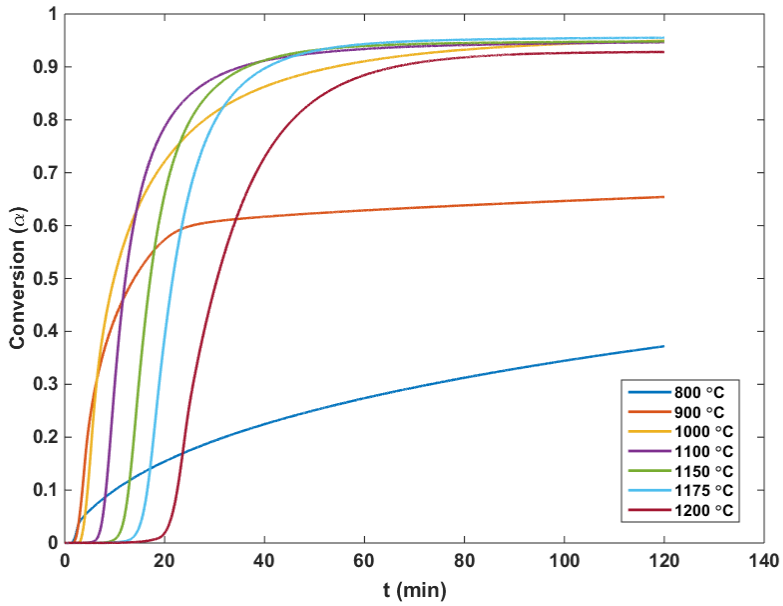

Figure 16: Carbonation conversion versus time under 1 bar of CO_2 for heat-treated SrO. A nominal 40 mg initial mass of 53-75 µm particles was used in each run.

The effect of particle size was also studied (Figure 18) by using heat-treated SrO particles at 1100C and 1 bar CO_2. No significant effect on the ultimate conversion or reaction kinetics was noticed. It is also notable that the induction time was not affected by particle size. This observation is significant in that it serves to discourage further investigation of smaller particle sizes as a means to improve material performance. Rather, the emphasis should be on preservation of the material capability over many cycles. These single carbonation runs show greater than 90% conversion, corresponding to at least 2000 kJ/kg (volume was not measured in these experiments).

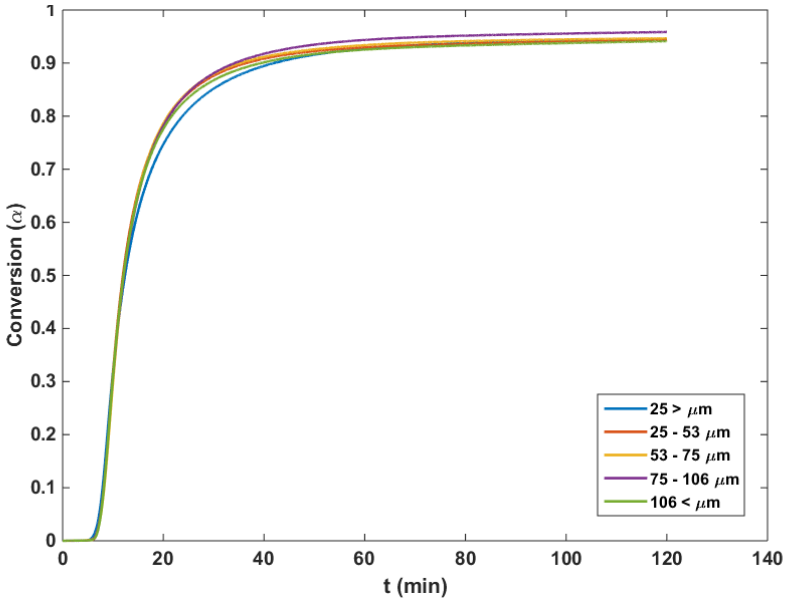

Figure 17: Carbonation at 1100°C and 1 bar CO_2 using various particle size ranges.

Subtask 1.2.2: Perform an isothermal study using TGA at several partial pressures of CO_2 to determine the dependence of the carbonation reaction on partial pressure of CO_2.

Pressure effects on carbonation were investigated by trials at 0.10, 0.25, and 1 bar CO_2. In the situations where the CO_2 was not 100%, nitrogen was used as the balance gas. Other parameters such particle size (53-75 um), and initial mass (~40 mg) were held constant. Each run was started with a fresh sample of heat-treated SrO. Figure 17 shows the effect of CO_2 partial pressure, P_{CO2}, on carbonation. P_{CO2} has a more dramatic effect at higher temperatures, whereas as lower temperatures the effect is minimal. This may be explained by the thermodynamics, as the equilibrium P_{CO2} increases with temperature. As a result, a mathematical dependence of reaction rate on temperature and pressure has yet to be determined.

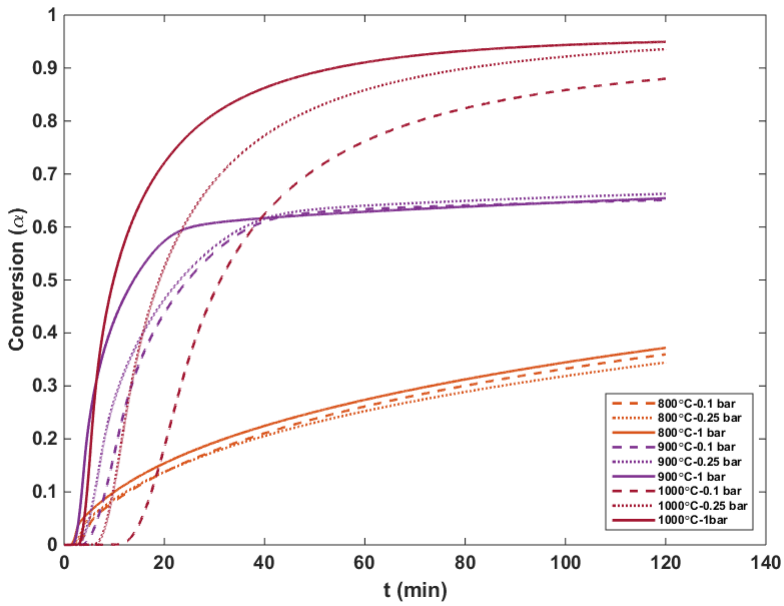

Figure 18: Carbonation conversion versus time under for heat-treated SrO under several P_{CO2}. A nominal 40 mg initial mass of 53-75 µm particles was used in each run.

Subtask 1.2.3: Develop a kinetic model incorporating appropriate rate law. Arrhenius parameters will be fit using a non-linear method, with uncertainty determined. The effect of morphological differences between dense pellet and SPF-G samples will also be accounted for.

The kinetics of CaO carbonation have been heavily studied previously. The general consensus is that carbonation occurs in three distinct regimes: induction, kinetic-controlled, and diffusion-controlled. The induction period refers to a period of time, sometimes several minutes, where a nucleation process must take place before a reaction can occur. Observation of this phenomena can be distorted if the experimental system has non-negligible "artifacts" such as time lag between actual reaction and the instrumentation tracking the reaction progress. The kinetic-controlled regime is where the maximum rate of reaction is observed, and thus is the most relevant to understanding the intrinsic reaction rates. Interestingly, Bhatia and Perlmutter [36] have found that the kinetics in this stage are not influenced by temperature, and thus do not obey an Arrhenius relationship. This has been noticed in our experimental results (see Figure 19), where the period of growth controlled by kinetics shows nearly identical slopes for all temperatures between 900 and 1150°C. The last stage is the diffusion-limited regime at which mass transfer limits the rate of reaction. A Random Pore Model has been used to explain this regime by many in the field, though it requires knowledge of the material structure.

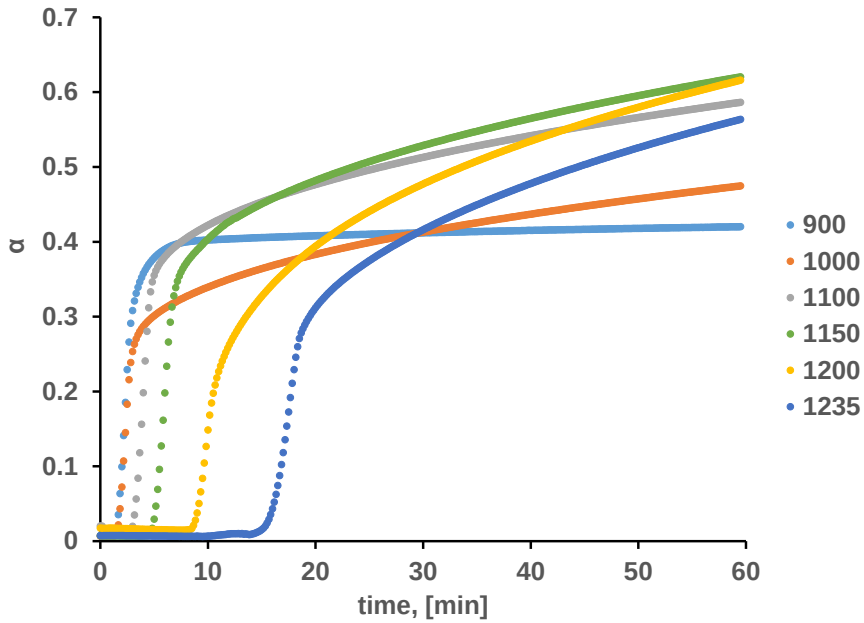

Figure 19: Extent of reaction, α, for six different isothermal runs for 1:1 mass ratio of SrO:$SrZrO_3$. From 900-1150°C, the reaction controlled portion has nearly identical slope.

The slightly less pronounced slope of the higher temperature runs at 1200 and 1235°C shown in Figure 16 are evidence that the apparent reaction rate is slowing down, which may be the result of reversibility.

Isothermal runs were performed with pure SrO as described in Subtask 1.2.1. The induction time, which is defined as the period between Figure 20 shows decreasing induction time with increasing P_{CO2}. Higher P_{CO2} are expected in a real process, which makes this effect less important. Conversely, high temperatures are desired in an actual implementation, and Figure 21 clearly shows increasing induction time with increasing temperature under 1 bar P_{CO2}. A model has been found that describes the dependence of induction time on temperature to within 95% confidence:

$$t_{induction} = 0.06387e^{0.003741T} + 5.103x10^{-10}e^{0.01998T}$$

where $t_{induction}$ is the induction time and T is the temperature in degrees Celsius [°C].

:

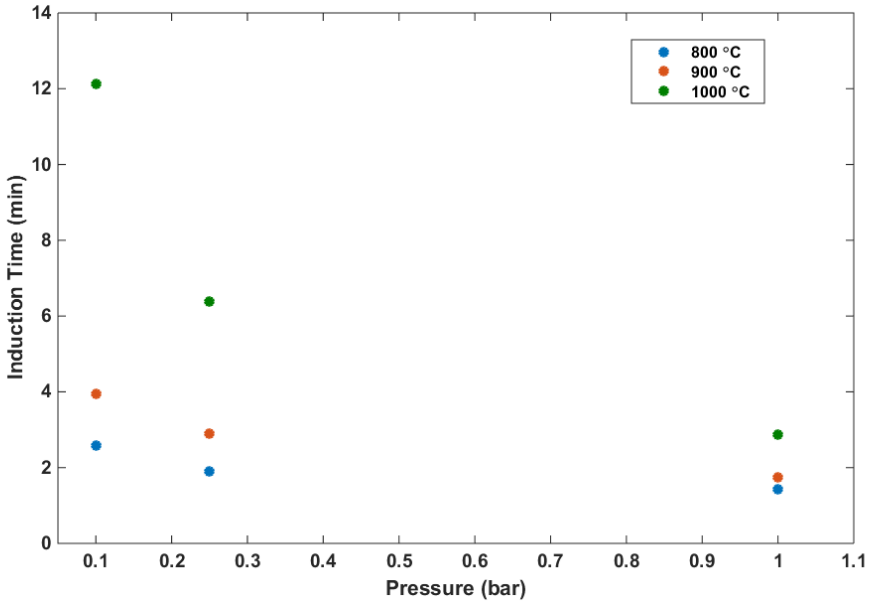

Figure 20: Effect of pressure on induction time.

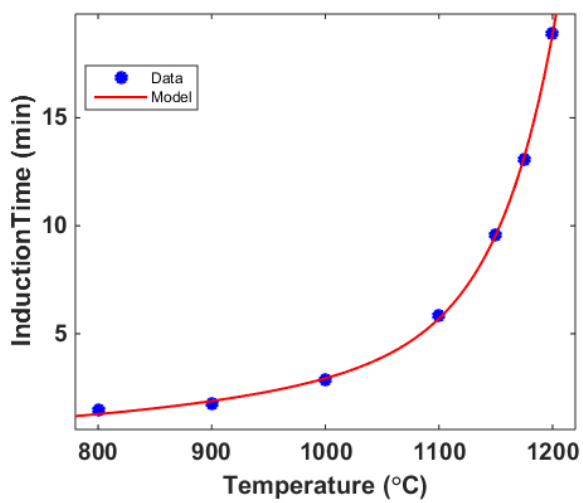

Figure 21: Induction time as a function of temperature under 1 bar CO_2.

Table 3: Temperature dependence of reaction rate and associated coefficients.

	$Rate\left[\min^{-1}\right] = AT^2 + BT - C$	
Coefficient	**Value**	**95% Confidence Interval**
A	-1.999e-06	[-2.544e-06, -1.453e-06]
B	0.004122	[0.003023, 0.00522]
C	-2.005	[-2.548, -1.461]

where T is again in degrees Celsius [°C]. Figure 22 shows the model and data describing the temperature effect.

The linear portion of the reaction corresponding to the kinetically-controlled regime was subjected to a least squares minimization. The resulting slopes were then plotted as a function of temperature (Figure 22). The apparent reaction rate does not obey a traditional Arrhenius relationship with temperature. Instead, a simple polynomial function has been fit to within 95% confidence intervals (see Table 3). The remaining reaction progress is controlled by the diffusion of CO_2 through the product layer ($SrCO_3$). Future work will describe this diffusion regime.

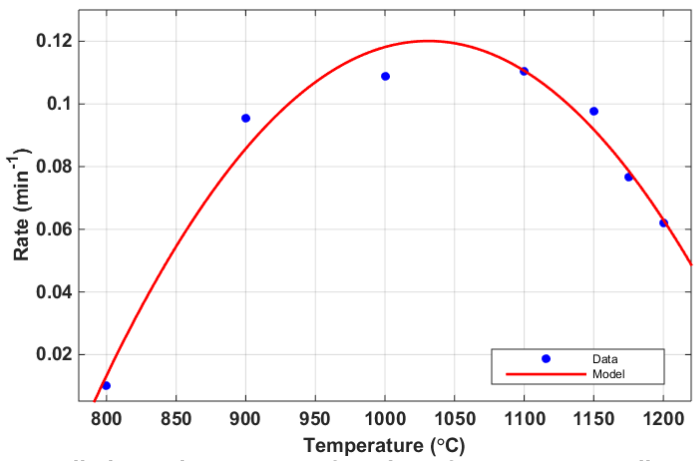

Figure 22: Kinetically-controlled reaction rate as a function of temperature. All experiments were carried out under 1 bar CO_2.

Milestone 1.2.1: Arrhenius parameters determined to within a 5 % uncertainty. Goodness-of-fit tests will be used to fit the model to the data and determine the uncertainty.

Given the apparently unconventional temperature dependence of the reaction, a polynomial was fitted to within 95% confidence intervals. More exploration of the reverse (decomposition) reaction is necessary to fully describe how reversibility plays into the apparent kinetics under a given temperature-pressure-gas environment scenario.

Milestone 1.2.2: The rate of SrO carbonation is greater than that of CaO carbonation at their respective optimum temperature at atmospheric pressure.

At this time, tabulation of rates from the experimentation conducted and comparison with literature has not been performed.

Task 1.3. A combination of conventional TGA and Solar TGA studies to obtain kinetic data for the decomposition reaction under a variety of conditions will be performed.

Subtask 1.3.1: Perform decomposition experiments using Solar TGA to acquire initial rate data at several different temperatures.

This has not been possible due to unavailability of the solar simulator.

Subtask 1.3.2: TGA studies of $SrCO_3$ at several decomposition temperatures with replication to produce data showing the progression of reaction extent versus time. Sensitivity to the partial pressure of CO2 will also be studied.

TGA/DSC study has been performed on the decomposition reaction using the same 1:1 mass ratio $SrO:SrZrO_3$ as used in Task 1.2. Figure 17 shows the extent of reaction for cycles carried out at six different isothermal decomposition temperatures between 1200 and 1300°C. A clear lag in decomposition rate at 1200°C is evident, while all other temperatures had sufficient kinetics to decompose completely in the allotted 60 minutes. A DSC trace is shown in Figure 18.

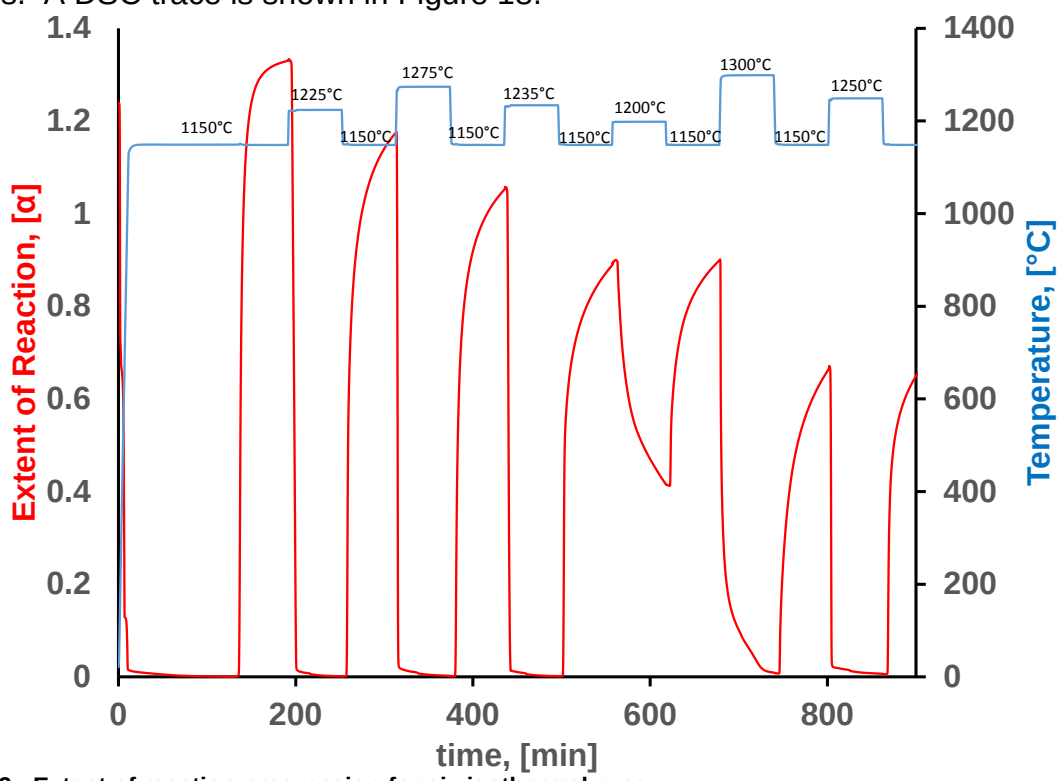

Figure 23: Extent of reaction progression for six isothermal runs.

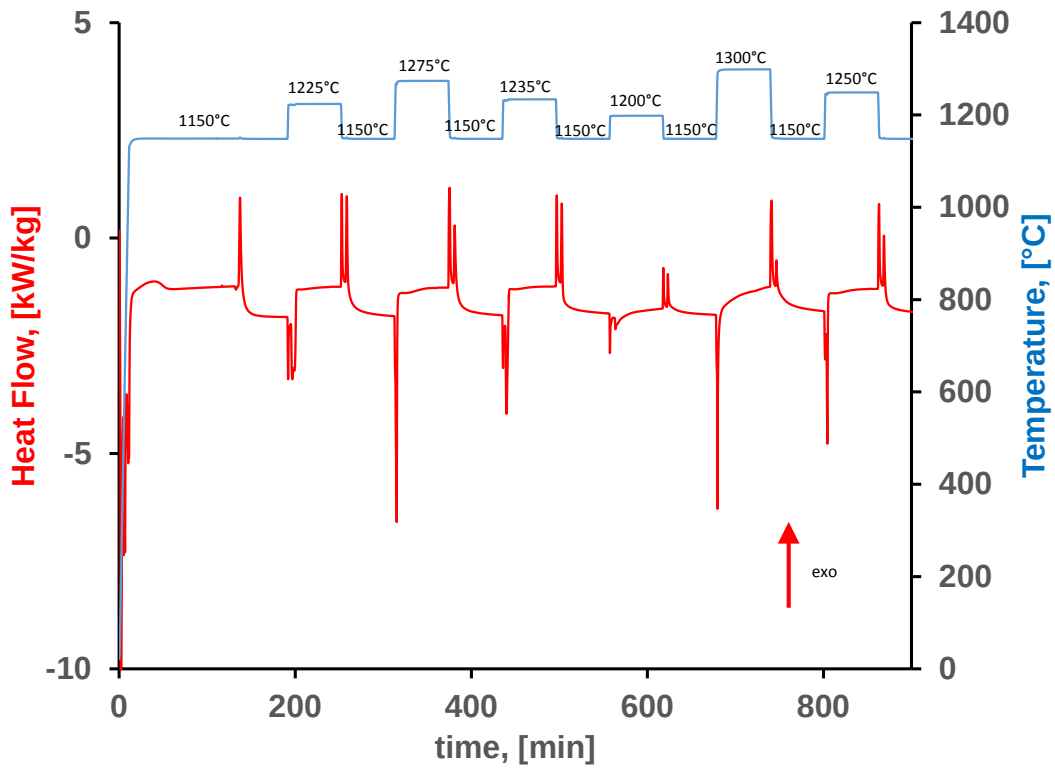

Figure 24: Heat flow of sample during six different isothermal runs. Carbonation occurred at 1150°C under 100% CO_2 and decomposition occurred under 100% N_2.

Milestone 1.3.1: Arrhenius parameters determined to within a 5% uncertainty. Goodness-of-fit tests will be used to fit the model to the data and determine the uncertainty.

A model has not yet been fit to the data since a more stable level of reactivity is desired.

Milestone 1.3.2: Ratio of peak rates at respective optimum temperatures for decomposition of $SrCO_3$ and $CaCO_3$ is ≥ 1.

Rates obtained in Task 1.3.1 will be compared to those published for $CaCO_3$.

Task 1.4: Develop a direct pore-level model for fluid flow, heat transfer, and chemical reaction inside porous $SrO/SrCO_3$ structure based on 3-dimentional (3D) real geometry obtained from micro-scale Computer Tomography (CT) in solid and fluid phases.

Subtask 1.4.1: Obtain tomography images for porous $SrO/SrCO_3$ structures at initial stage and after multiple cycles; segmentation and image processing to render representative 3D structures of samples.

SrO samples prepared with the pore formation method (SrO is the only solid phase after burning off of graphite) were scanned at the Advanced Photon Source (APS) beamline of Argonne National Laboratory (10/27–28/2014). SrO samples with supporting material (e.g., SrYSZ, $SrZrO_3$, $SrTiO_3$, and $SrAl_2O_4$, two solid materials coexist in the structure) were scanned at APS during 02/07-08/2015. For each case, samples before and after the carbonation-decomposition cycling were imaged for comparison. 3D rendering structures were obtained after image processing.

The resolution of the facility is 0.65 µm. The raw tomographic data was processed using TomoPy image processing package [37]. The cubic middle section of size 1600x1600x1600 voxels from each reconstructed 3D image is chosen for the analysis of each structure. 2D slices and 3D reconstructed representations for these samples before and after cycling are presented.

Table 4: 2D & 3D representation and properties of SrO samples with pore-formation and no supporting material.

	Sample 8 before cycling	Sample 8 after 5 cycles	Sample 7 after 5 cycles
2D	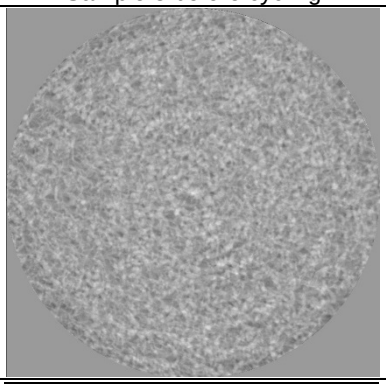	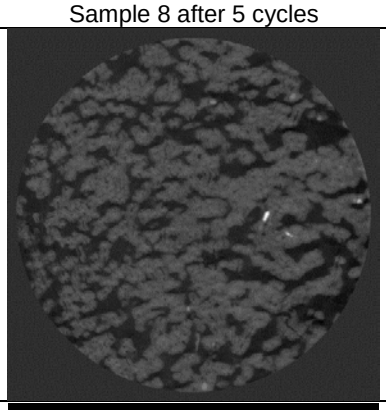	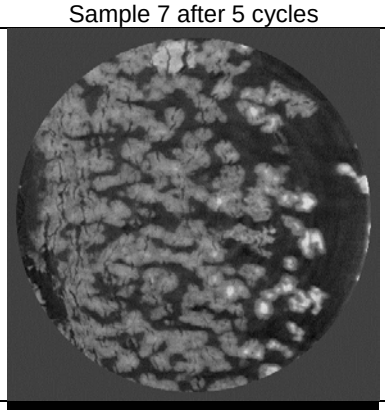
3D	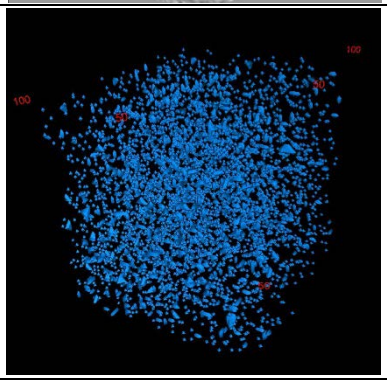	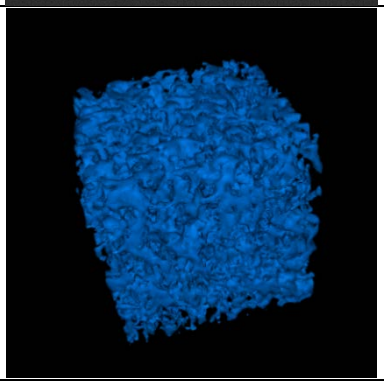	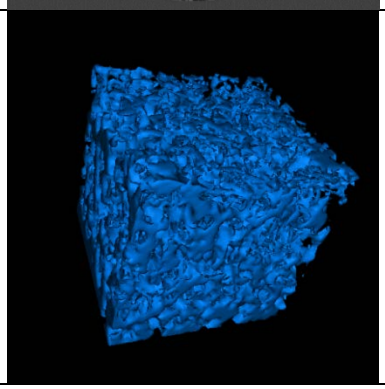
ε	0.56	0.38	0.45
SSA [m^{-1}]	8.01x104	3.06x104	4.24x104

Table 5: 2D and 3D representation and properties of SrO samples with supporting material.

Material	SrO + SrYSZ (1:1 mass ratio)	SrO + SrYSZ (2:3 mass ratio)	SrO +$SrZrO_3$ (1:1 mass ratio)
2D (Before Cycling)	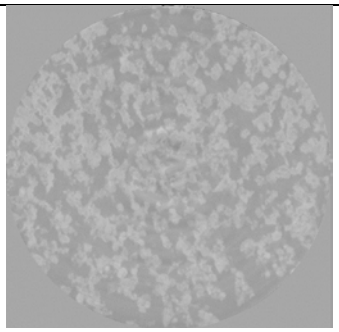	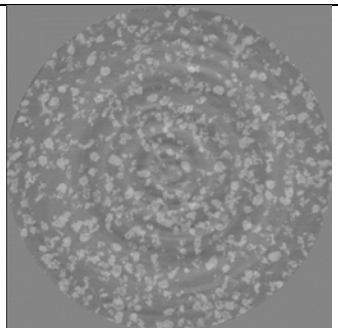	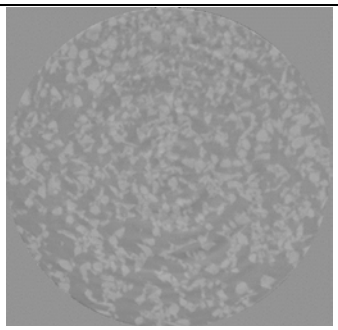
3D (Before Cycling)	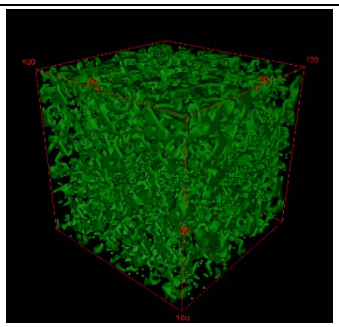	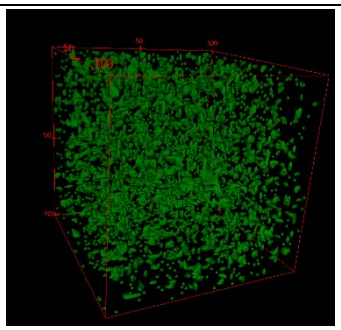	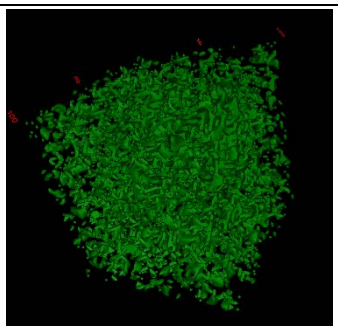
ε	0.51	0.72	0.59
SSA [m^{-1}]	5.27×10^4	4.41×10^4	5.05×10^4
2D (After Cycling)	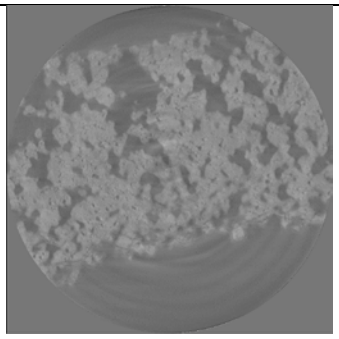	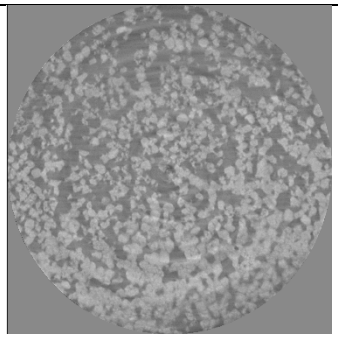	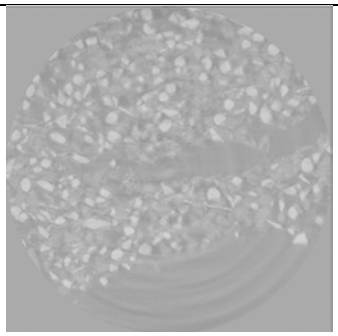
3D (After Cycling)	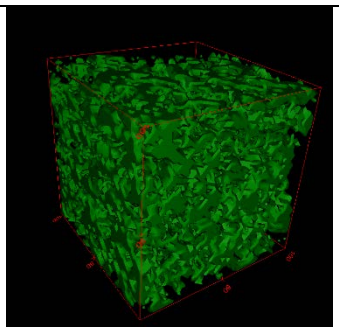	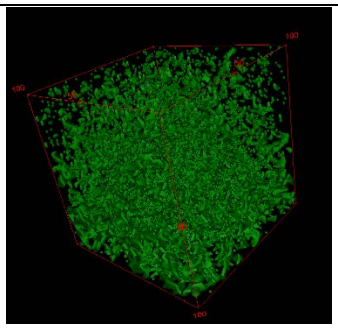	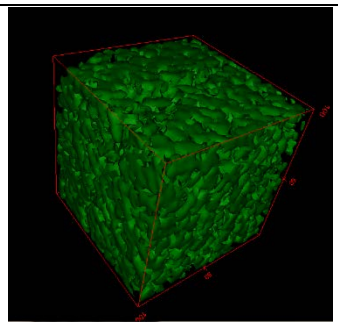
ε	0.38	0.53	0.59
SSA [m^{-1}]	4.38×10^4	5.35×10^4	5.36×10^4

Table 4 in the above shows the images of the respective 2D slice and 3D structures for three different samples prepared with pore formation together with the computed porosity (ε) and specific surface area (SSA) values [m^{-1}]. The particle sizes for Samples 7 are 106-125 µm (SrO) and 25-38 µm graphite; and for Sample 8 both SrO and graphite particles are in the range of 25-38 µm. Table 5 shows the images of respective 2D slices and 3D structures for three different samples with different supporting materials. The particle size is in the range of 38-63 µm for all these cases.

The results of sample characterization in Table 4 and Table 5 show that in general the samples with supporting material show better structural integrity and less loss of porosity and surface area due to sintering during cyclic operations.

In all cases the porosity of the sample decreased after cycling. With supporting material the uniformity of the structure is maintained and less sintering is observed. The two different solids in the samples with supporting material can be distinguished to a certain extent in the 2D images. Effort has been devoted to better identify the differences and reconstruct 3D representations that have two different solids.

Subtask 1.4.2: Simulate the fluid flow inside the porous structure in a range of typical Reynolds numbers to obtain the permeability and Forchheimer constant.

For a porous structure, the permeability **K** and Forchheimer constant **β** are computed for a given pressure gradient ∇p and the average velocity ***U*** according to the modified Darcy's model with a non-linear term representing fluid inertia:

$$\left(\mu \mathbf{K}^{-1} + \rho \boldsymbol{\beta} \,|\, \mathbf{U} \,|\right) \mathbf{U} = -\nabla\, p \tag{1}$$

where μ and ρ are the fluid viscosity and density, respectively. Based on the experimental conditions intended for obtaining high chemical conversion, the Reynolds number for the fluid flow in the porous $SrO/SrCO_3$ structure is very small. The pore level simulations are conducted for the pore-scale Reynolds number ranging from 0.1 to 1.1. The permeability and Forchheimer constant for the three samples in Table 4 are computed using the lattice Boltzmann equation (LBE) method with a parallelized in-house code and the results are listed in Table 6.

Table 6: Permeability & Forchheimer constants in three directions for samples in Table 4.

Sample	Flow direction	Forchheimer constant β (unit: m^{-1})	Permeability K (unit: m^2)
#8 before cycling	x	-59504 ± %92	8.14E-11 ± %0.14
	y	46244 ± %166	8.33E-11± %0.20
	z	245148 ± %36	7.95E-11 ± %0.21
#8 after cycling	x	300310 ± %12	9.7757E-11 ± %0.1
	y	484950 ± %13	9.5204E-11± %0.1
	z	292670 ± %11	1.4579E-10 ± %0.1
#7 after cycling	x	393172 ± %8.6	2.6688E-10 ± %0.75
	y	419150 ± %8.4	2.3862E-10 ± %0.65
	z	370349 ± %7.2	2.0300E-10 ± %0.36

The permeability of the porous SrO/$SrCO_3$ structures is close to isotropic since the deviation is less than 10% in each flow direction. The results for β show higher uncertainty since it was determined with weak nonlinearity of the flow field for which the first term in Eq. (1) dominates the left-hand-side of the Darcy's law.

Subtask 1.4.3: Simulate the heat transfer including conduction, convection and radiation in porous media to obtain the effective heat transfer coefficient and thermal conductivity.

The effective thermal conductivity, k_{eff}, of a porous structure can be expressed as

$$k_{\text{eff}} = k_{\text{cond}} + k_{\text{rad}}\,, \tag{2}$$

where k_{cond} is the contribution due to pure heat conduction within the fluid and solid phases, and k_{rad} is the radiation component, which is significant at high temperatures. Here the radiation component is modeled using the Rosseland diffusion approximation:

$$k_{\text{rad}} = \frac{16\sigma T^3}{3\beta_r}\,, \tag{3}$$

where σ is the Stefan-Boltzmann constant, and β_r is the mean extinction coefficient of the structure that is determined by the 3D geometry of the structure. The extinction coefficient used in this work is the average of the three correlations given in Table 7 where ε is the porosity, d is the mean diameter of spheres, and $\beta_u = 3(1-\varepsilon)/d$.

Table 7: Correlations for dependent scattering approximation of the extinction coefficient for packed beds.

Kamiuto [38]	$\gamma_2 = \frac{\beta}{\beta_u} = 1 + \frac{3}{2}(1-\varepsilon) - \frac{3}{4}(1-\varepsilon)^2$	$\varepsilon < 0.921$
Singh & Kaviany [39]	$S_r = \frac{\beta}{\beta_u} = 1 + 1.84(1-\varepsilon) - 3.15(1-\varepsilon)^2 + 7.20(1-\varepsilon)^3$	$\varepsilon > 0.3$
Hendricks & Howell [40]	$\beta = \frac{4.4(1-\varepsilon)}{d}$	Reticulate porous structure

The temperature dependency of k_{cond} for both solid and gas phases is considered to obtain k_{eff} of the SrO structure as a function of temperature. The pure solid SrO thermal conductivity k_s decreases with T while the gas conductivity k_f of CO_2 increases with T. Their temperature dependence correlations are $k_s = 17.73/(1+0.0014T)$ and $k_f = -3.93\times10^{-4} + 1.02\times10^{-4}T - 4.86\times10^{-8}T^2 + 1.52\times10^{-11}T^3$ (T in ºC) [41]. Figure 25 shows the variation of k_{eff} with the average temperature of the structure in different directions for the three samples in Table 4. The radiation part is applied for both solid and gas phase similarly. The results in Figure 25 confirm that k_{eff} of the SrO structure increases about twice when it sinters after the carbonation-decomposition looping for 5 cycles. It is also noticed that the differences of k_{eff} values in the three directions increase after cycling, indicating that the structure is not as uniform as it was before cycling.

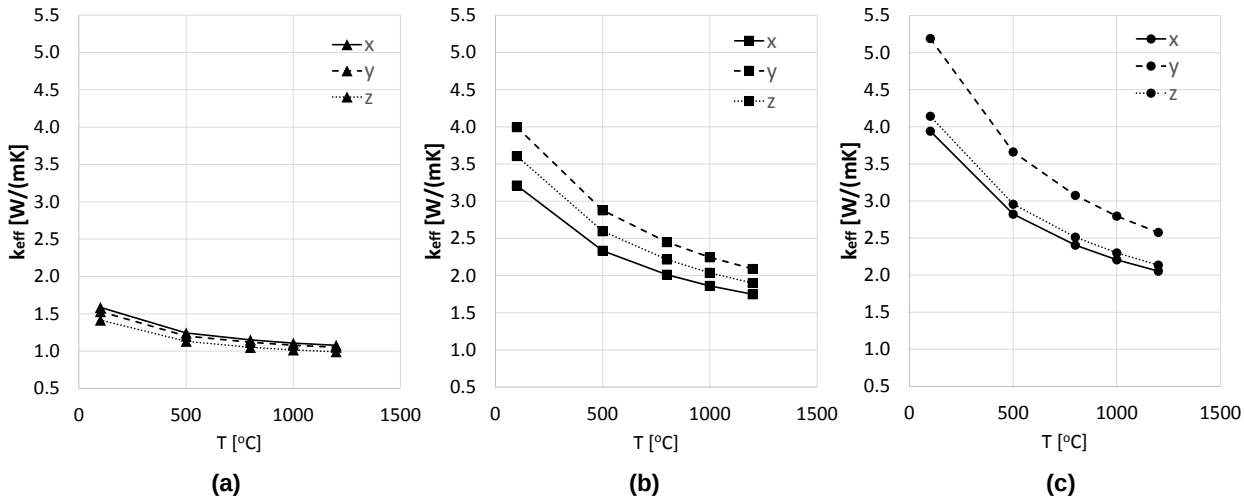

Figure 25: Effective thermal conductivity k_{eff} as a function of temperature for (a) Sample 8 before cycling, (b) Sample 8 after 5 cycles, and (c) Sample 7 after 5 cycles.

The estimated extinction coefficient β based on the porosity and mean particle size of the SrO structures is relatively large. Consequently the radiative thermal conductivity k_{rad} compared to k_{cond} is not significant even at high temperatures. In order to investigate the effect of β on k_{eff}, three different values of β = 5000, 10000, and 50000 m^{-1} are used for heat transfer simulations using the geometry of Sample 8 before cycling. The results are shown in Figure 26.

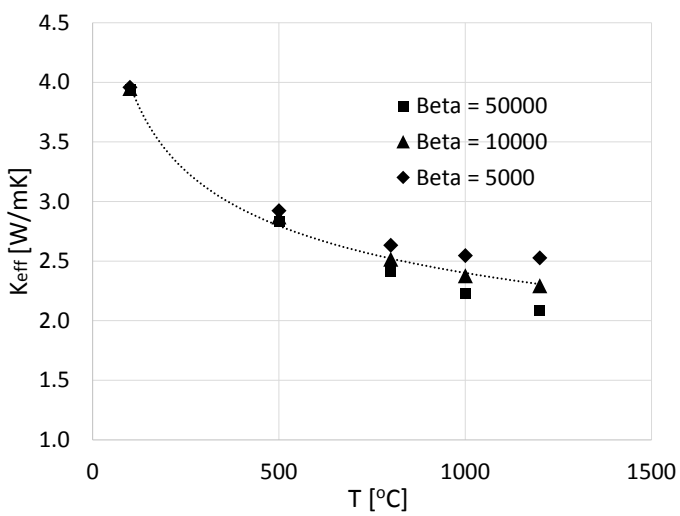

Figure 26: k_{eff} as a function of temperature for different exticntion coefficient β values using the same geometry of Sampel 8 before cycling.

It is observed in Figure 26 that for radiative heat transfer to be important, the porosity and pore size of the structure need to be increased. This insight can be used to guide future material structure design with the objective of enhancing heat transfer from the heat generation due to SrO carbonation to the working fluid, especially at the relatively larger scale such as the tubular bed reactor.

Subtask 1.4.4: Validate the simulated transport properties with available data in the literature and experimental measurements.

Six SrO samples prepared with pore-formation and different particle sizes have been shipped to two companies for thermal conductivity measurement. Three samples were sent to Setaram where low temperature measurement will be conducted at T = 25, 50, 100, and 150 ºC. The other three samples were sent to Netzsch where high temperature measurement up to 1100 ºC will be conducted. The results are expected to be ready in 3 weeks. Direct comparison between pore-scale simulation and experimental measurement will be conducted when the measurement results are obtained.

The effective thermal conductivity of Sample 8 before cycling (see Table 4) is compared with the empirical models available in the literature and the results are shown in Figure 27. Cleary the present results are well within the limits bounded by the parallel and serial slab models. Also for larger k_s/k_f values, the present results are close to that represented by the Schuetz-Glicksmann model.

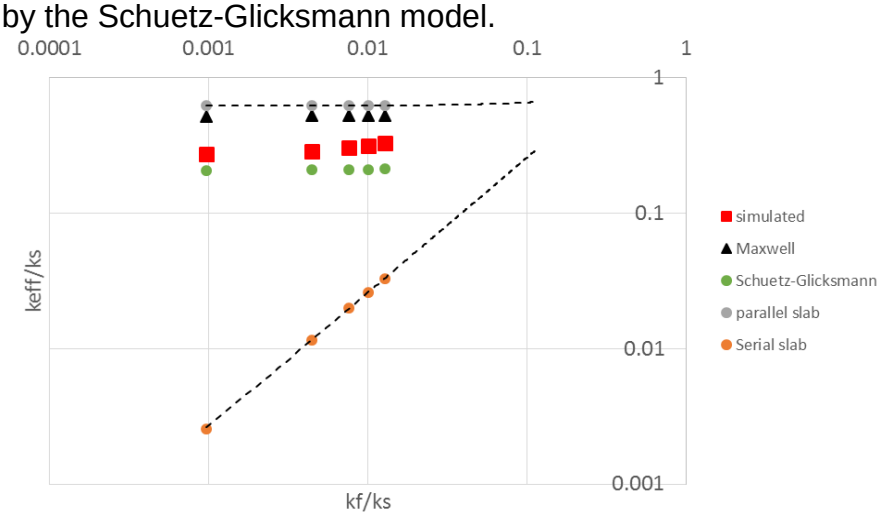

Figure 27: Comparison of k_{eff} values using different models in the literature [42].

Subtask 1.4.5: Simulate the transient chemical reaction coupled with fluid flow in the 3D structures of different porosities to determine the optimal structure that is able to produce the highest volumetric heat flow rate.

In this section we report the results of simulation of SrO carbonation reaction process in the gas flows coupled with energy and species transport.

The governing equations to model the fluid flow, energy equation, species transport, and carbonation process are as follows. The flow field in the gas phase obeys the impressible Navier-stokes equation.

$$\nabla \cdot \mathbf{u} = 0\,, \tag{4}$$

$$\rho\left(\frac{\partial \mathbf{u}}{\partial t} + \mathbf{u}\cdot\nabla\mathbf{u}\right) = -\nabla p + \mu\nabla^2\mathbf{u}\,, \tag{5}$$

The species transport equations are

$$\frac{\partial C_{CO_2}}{\partial t} + \nabla\cdot\left(\mathbf{u}C_{CO_2}\right) = D_g\nabla^2\left(C_{CO_2}\right) \text{ in the gas phase,} \tag{6}$$

$$\frac{\partial C_{CO_2}}{\partial t} = D_s \nabla^2 \left(C_{CO_2} \right) - S \text{ in the solid phase,} \qquad (7)$$

where the volumetric energy sink term S due to carbonation reaction is given by a chemical kinetics $S = kf\left(\alpha\right)C_{CO_2}$ with k being the rate constant and $f\left(\alpha\right)$ a function of the conversion factor, α, of SrO.

The energy transport equations are

$$\rho_f C_{p,f} \frac{\partial T}{\partial t} + \nabla \cdot \left(\mathbf{u} T \right) = K_f \nabla^2 T \text{ in the gas phase,} \qquad (8)$$

$$\rho_s C_{p,s} \frac{\partial T}{\partial t} = K_s \nabla^2 T + G \text{ in the solid phase,} \qquad (9)$$

where *G* is the volumetric heat generation rate due to the conversion of SrO:

$$G = C_{SrO}\big|_{\alpha=0} \Delta H \frac{d\alpha}{dt}, \qquad (10)$$

where $C_{SrO}\big|_{X=0}$ describes the molar concentration of SrO when $\alpha = 0$, namely no conversion has occurred, $\Delta H = 234\ kJ/mol$ is the enthalpy change per mole of SrO being converted, and $\frac{d\alpha}{dt}$ is the rate of change of the conversion factor.

The present simulation is similar to a recent publication [43] which is for pore scale coupled gas-solid reaction involving iron oxidation. During the study in this reporting period, it is found that the volumetric heat flow rate in the carbonation process is highly sensitive to the carbonation kinetics in terms of the rate $\frac{d\alpha}{dt}$. One must recognize that $\frac{d\alpha}{dt}$ as a function of α determined in a lab typically is based on a lumped reaction model. It is based on the average α of a bed consisting of many partially reacted particles, not the local intrinsic value of α, from TGA measurements. The kinetics model needed in the current simulation involves the local conversion α of SrO and local concentration of CO_2 being diffused into SrO that both vary in space during the carbonation. Thus the kinetics data in Task 1.2 should be used only as a guide to determine the intrinsic rate.

The pore scale simulation results further reveal that the volumetric heat flow rate is strongly dependent upon two parameters: the solid phase mass diffusivity D_s which characterizes the speed of CO_2 diffusing into SrO and chemical kinetics that governs the rate of the carbonation reaction. The mass diffusivity D_s is not available in the literature. From the SEM images reported in Subtask 1.1.2, structure of the "particle" even on the 20 μm scale is still very complex and show some level of porosity inside the "particles" that we intend to simulate. Thus the diffusivity is mostly likely much higher than that for pure solid. A design of experiment to determine D_s value is underway. Observing that a rapid decay of reaction rates occurs in the experiment, we model the pore-scale chemical kinetics in the following form

$$S = k\left(1+\alpha\right)^{\beta} C_{CO_2}, \qquad (11)$$

where the reaction rate k and power β are parameters to be determined by matching the experiment results to a reasonable extent.

Two Dimensional Simulations

The structure of the present study consists of 2-D cylindrical SrO particles together with supporting (but non-reacting) $SrZrO_3$ particles shown below. In the meantime, the code for 3D parallel computation is currently under the way to implement the kinetics model. The 3-D simulation will take significantly more CPU time.

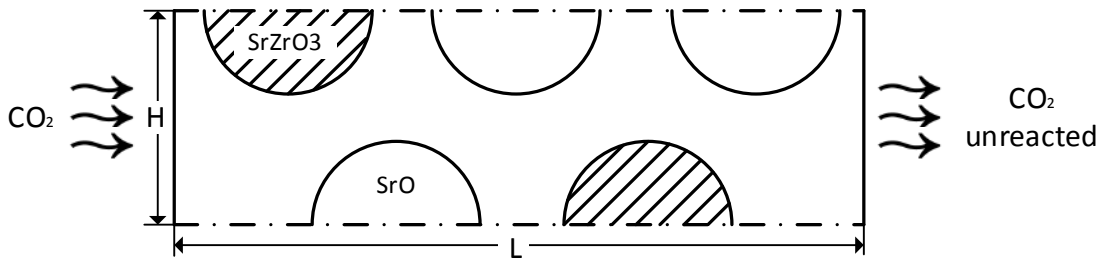

Figure 28: Schematic depicture of the computational domain.

As shown in Figure 28, the idealized geometry is considered to be an array of cylinders with the same radius r in the computation domain of which the top and bottom lines are the axis of symmetry. The size of the domain is $1300\ \mu\text{m} \times 370\ \mu\text{m}$. To be consistent with the experimental configuration, two semi-cylinders (shown in bold line) out of five are treated as supportive material that does not participate in the reaction. Symmetry conditions are imposed at the boundaries in the vertical direction.

The flow field is solved to obtain a steady-state velocity field for a given pressure gradient with periodic boundary condition in the flow direction. The magnitude of the pressure gradient is chosen such that the resulting Reynolds number matches the experimental condition (*Re* = 0.012). Since there is always sufficient CO_2 present and loss of CO_2 due to carbonation reaction is very small in the gas stream, the effect of reaction on the velocity field is neglected. The species and energy transports are solved by time marching. A flow of CO_2 under the condition of 1100 °C and 1 atm is introduced at the inlet to the porous structure that has been preheated to 1100 °C. The volumetric heat flow rate is calculated based on the entire heat generation produced by the carbonation reaction within the solid phase. Simulations end at *t* = 5 minutes.

For parametric investigation, a baseline case with following parameters is chosen first: $r_0 = 150\ \mu\text{m}$, $D_s = 2\times10^{-9}\ \text{m}^2/\text{s}$, $k = 2.25\ \text{s}^{-1}$ and $\beta = 10$. A visualization of SrO conversion at *t* = 1, 2 and 5 min is given in Figure 29. A reaction layer is formed due to the carbonation diffusing from the surface of the cylinders. The extent of conversion and the thickness of the reaction layer increases with time simultaneously. For this case, the thickness of reaction layer is around $40\ \mu\text{m}$ in 5 minutes.

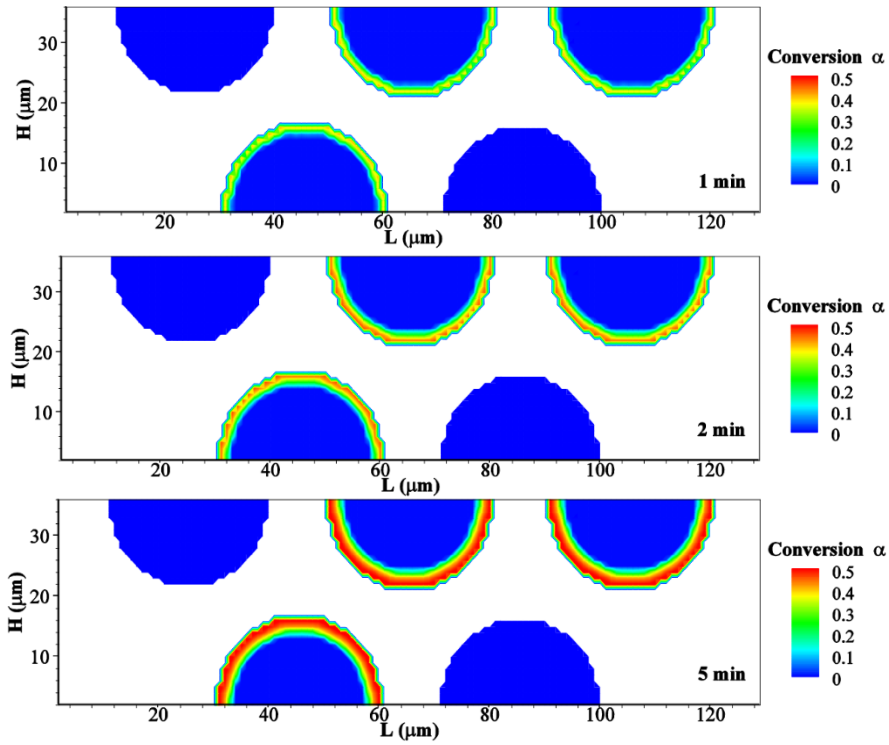

Figure 29: Conversion contours of SrO at *t* = 1, 2, and 5 min.

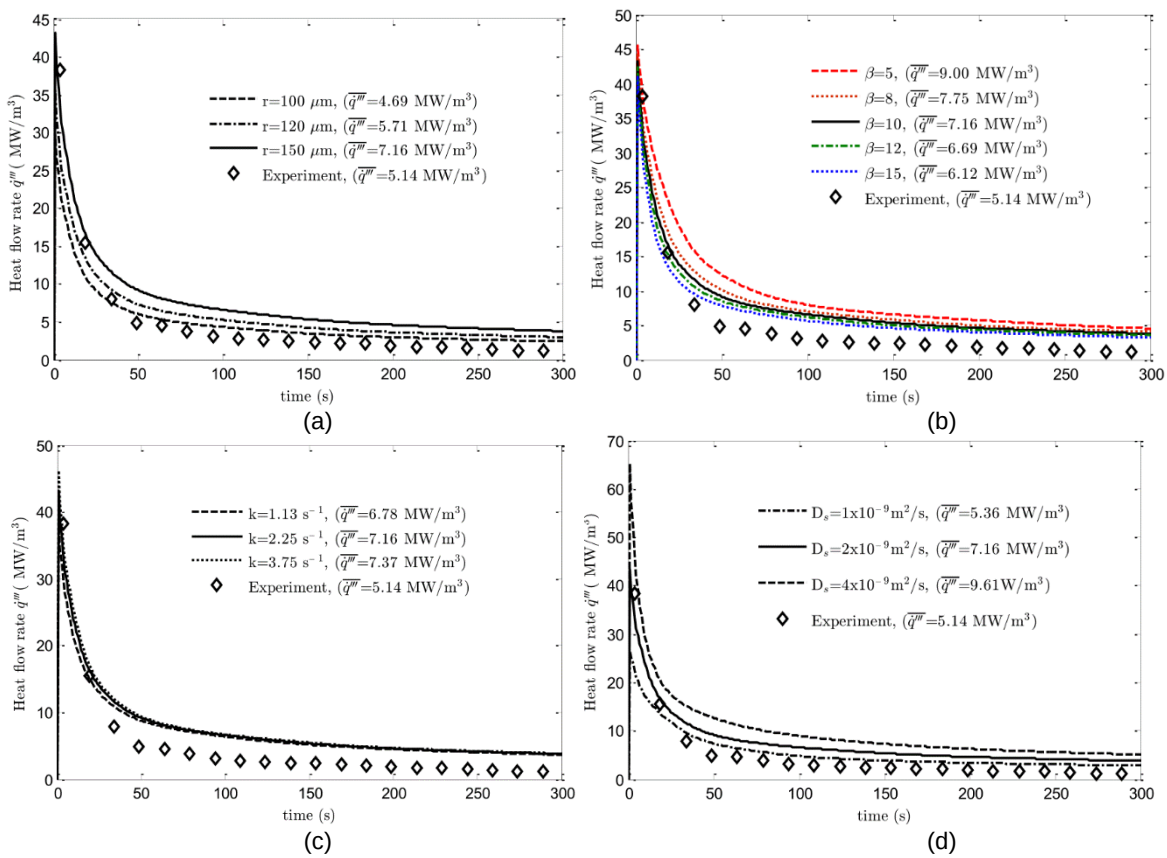

Figure 30: Comparison of volumetric heat flow rate for different parameters: (a) radius *r*, (b) power *β*, (c) reaction rate *k*, and (d) mass diffusivity D_s.

Using this case as the base case for reference, a control variable method is employed to investigate the dependence of volumetric heat flow rate by various radii of particles $r = \{100, 120, 150\}\ \mu\text{m}$, solid mass diffusivity $D_s = \{1\times10^{-9}, 2\times10^{-9}, 4\times10^{-9}\}\ \text{m}^2/\text{s}$, reaction rate k = {1.13, 2.25, 3.75}s^{-1} and $\beta = \{5, 8, 10, 12, 15\}$. These values of radius correspond to porosity ε = 0.769, 0.680, and 0.526; and different radii are used to represent the effect of porosity or surface area. Figure 30 compares the volumetric heat flow rate using different parameters along with the experiment result. The trend follows that of the experimental data. The 5-minute averaged volumetric heat flow rate, $\overline{\dot{q}'''}$, is obtained by integrating over 5 minutes for each curve in the graph.

The effects of each parameter on $\overline{\dot{q}'''}$ are examined in order to optimize the structure in the future: (a) higher $\overline{\dot{q}'''}$ is obtained with a larger radius particles, which indicates that a less porous structure with more surface area; (b) a smaller β, essentially a slower decay of reaction rate with respect to the conversion, results in a higher $\overline{\dot{q}'''}$, in particular during the initial period when the most rapid carbonation occurs; (c) the reaction rate constant k seems to have a limited influence on the result in the range considered and a larger range needs to be investigated in the future work to further understand its effect, and (d) a larger mass diffusivity of solid phase allows more CO_2 to diffuse deeper into the solid so that more SrO can participate in the exothermic reaction. Furthermore, the solid diffusivity plays a crucial role in affecting the peak heat flow rate.

To conclude from this parametric investigation, the goal of average volumetric heat flow rate ≥ 4.0 MW/m^3 during the first 5 minutes can be achieved in this idealized structure.

Because of the lack of information on the solid diffusivity of SrO and on the intrinsic chemical kinetics on the pore scale and also because the kinetics data based on lumped model only becomes available shortly before the present report is due, 3D simulations, which will take significantly longer CPU time, have not been performed for parametric studies at the time of submitting this report. However, the results from the 2D simulations are rather encouraging in terms of meeting the goal of achieving higher than 4.0 MW/m^3 average volumetric heat flow rate in the first 5 minutes. The insight from 2D simulations will also make the 3D simulations more efficient.

Three dimensional simulations

In this section, a 3-D pore-level simulation results of SrO carbonation reaction process in the gas flows coupled with energy and species transport using lattice Boltzmann equation (LBE) method are presented.

As a validation of the 3-D parallel code, its volumetric heat flow rate generated by SrO carbonation process is plotted along time and compared with the one obtained from 2-D simulation using identical parameters. As shown in Figure 31, the 3-D simulation result exhibits a good agreement with the 2-D simulation.

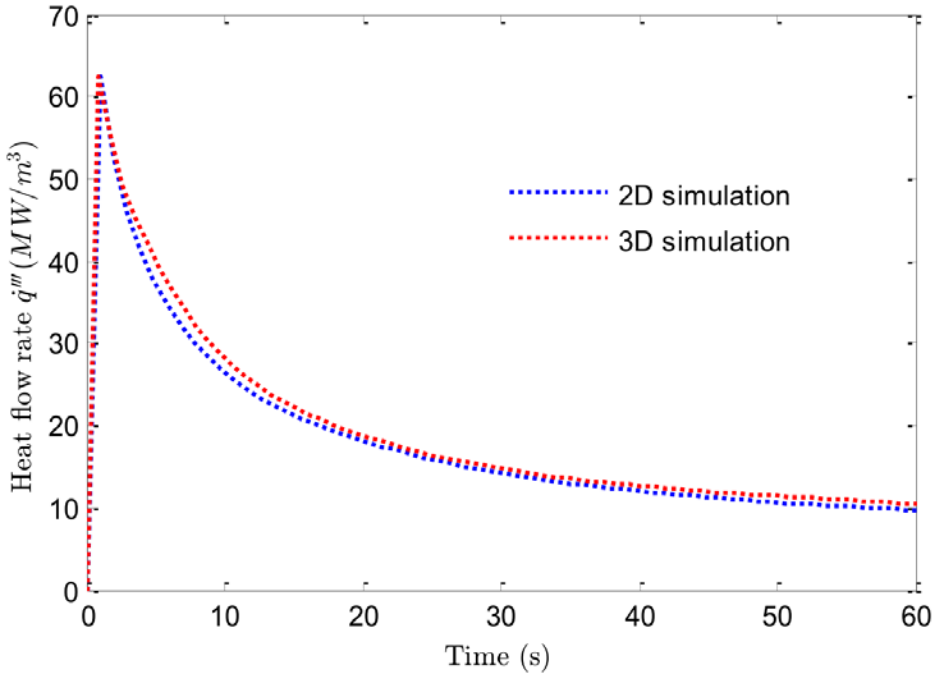

Figure 31: Comparison of 2D and 3D simulation results.

Recall that the parametric study concerning solid phase mass diffusivity D_s and chemical kinetics has been performed in the last reporting time. The motivation of the current study is to investigate the effects of different geometric configurations on the behavior of the carbonation process, particularly the volumetric heat flow rate generated along the chemical reaction in the first 1 min. A control variable method is employed to investigate the influence of various geometric parameters, including SrO particle size d_1, SrYSZ particle size d_2, and the characteristic length between particles L (center to center). Several numerical cases are performed. Table 8 summarizes the parameters used in the simulation with the corresponding porosity and reactive surface area per unit volume S_1/V. The mass diffusivities of solid and gas phases used for all cases are: $D_s = 2.0\times10^{-9}\,\mathrm{m^2/s}$ and $D_f = 4.4\times10^{-6}\,\mathrm{m^2/s}$, and the pore-scale chemical kinetics are considered to be

$$S = 20(1+\alpha)^{10} C_{CO_2}, \quad [\text{unit: } mol\cdot m^{-3}\cdot s^{-1}], \qquad (12)$$

where α denotes the conversion factor of SrO.

Table 8: Geometric parameters used in simulation.

Case No.	Geometry	d_1 (μm)	d_2 (μm)	L (μm)	Porosity	S_1/V (μm^{-1})
1	Config.1	90	90	100	0.618	0.0063
2	Config.1	90	70	100	0.719	0.0063
3	Config.1	90	50	100	0.776	0.0063
4	Config.1	72	72	80	0.618	0.0080
5	Config.1	54	54	60	0.618	0.0114
6	Config.2	140	140	100	0.707	0.0038
7	Config.3	140	76	100	0.619	0.0038

Figure 32 shows the three geometric configurations considered in the present study. The structure consists of spherical SrO particles together with supporting (but non-reacting) SrYSZ particles. In configurations 1 and 2, SrO and SrYSZ particles are aligned in a non-staggered and staggered pattern respectively, while in configuration 3 SrO particles are surrounded by supporting particles. Note that only a single period of the structure is shown below, and the computational domain is comprised of three such periods in series. Through Case 1 to Case 3, the geometry of the structure remains the same while only the size of supporting particles is different. Case 4 and Case 5 keep the same ratio of each geometric parameter as in Case 1 but all sizes are shrank by 20% and 40% respectively. Furthermore, staggered structure and surrounded structure are applied in Cases 6 and 7, where the size of SrO particle is chosen such that the total mass of SrO per volume is the same as of Case 1.

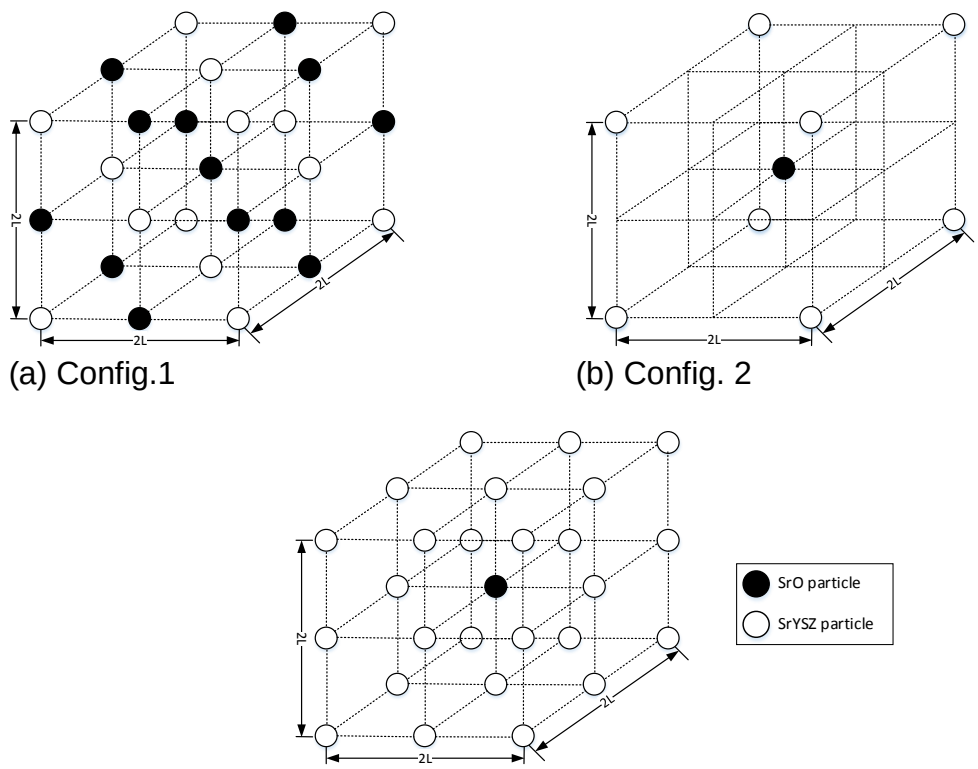

(a) Config.1 (b) Config. 2

(c) Config. 3

Figure 32: Schematic depicture of the geometric configurations.

Figure 33 shows the comparison of the volumetric heat flow rates for different cases: (a) through Case 1 to Case 3, slightly higher heat flow rate $\dot{q}'''$ is observed with a smaller size of SrYSZ particles, which is probably caused by a larger porosity. However, the amount becomes less significant as the carbonation process proceeds; (b) More CO_2 is allowed to participate in the exothermic reaction with SrO particles in Cases 4 and 5 due to a larger reactive surface area available, which provides a greater amount of heat flow rate, especially at the initial stage; (c) Despite the total mass of SrO per volume being the same, a much smaller amount of heat has been generated for the other two geometric structure in Cases 6 and 7, which can also be explained by the surface area effect.

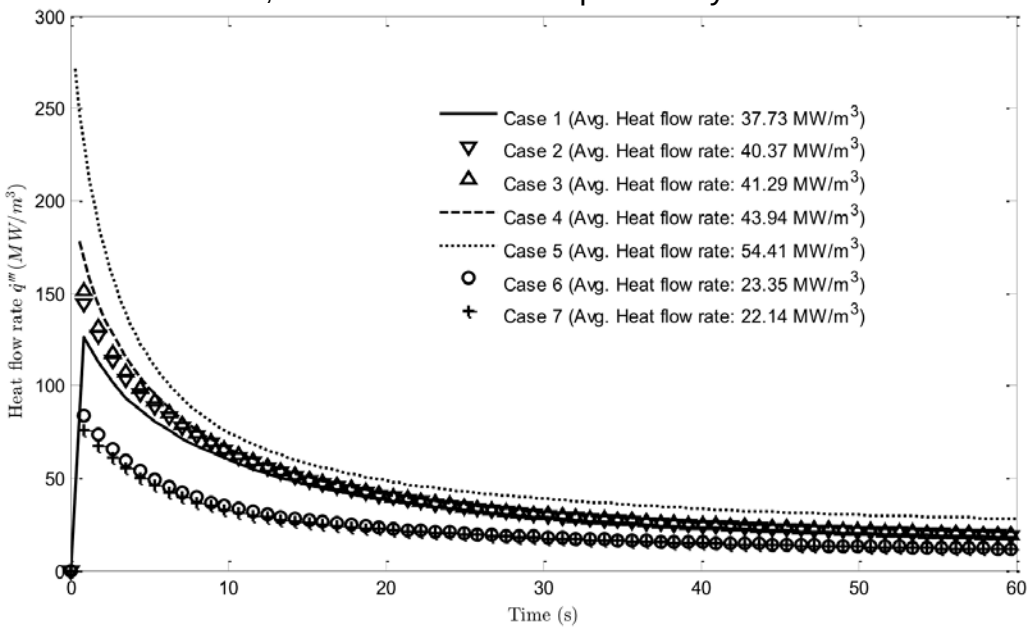

Figure 33: Comparison of volumetric heat flow rate for different cases.

To estimate the effects of porosity ε and reactive surface area per volume S_1/V quantitatively, a regression technique is used to model the average heat flow rate ($\bar{q}'''$ in MW/m^3) as a function of ε and S_1/V. The result gives

$$\bar{q}''' = 2.367\varepsilon + 13.97\left(S_1/V\right) - 0.4698\varepsilon^2 + 1.605\varepsilon\left(S_1/V\right) - 2.211\left(S_1/V\right)^2 + 40.33, \qquad (13)$$

where ε is normalized by mean 0.6679 and standard deviation (STD) 6.543X10^{-2} and S_1/V is normalized by mean 6.557X10^{-3} and standard deviation (STD) 2.612X10^{-3}. The coefficient of determination R^2=0.9986 and root mean square error RMSE=1.046 guarantee the goodness of this fitting. With the high order correction being neglected, the fitting model suggests that the value of reactive surface area is around 6 times more important as for the average heat flow rate. The insights from the present model can be applied for the experimental design.

Task 1.5: Using input from both the literature and prior milestones, a system-level analysis will be performed to determine overall $SrO/SrCO_3$ system process viability. A process flowsheet will be used to quantify the energetic and exergetic efficiency, as well as the time required to store CO_2. Of specific interest is the matching of the rates of various sub-processes (heat transfer, chemical kinetics, absorption, etc).

Subtask 1.5.1: Create process flowsheets for different configurations based on existing process flow diagram.

Subtask 1.5.2: Using process flowsheets, carry out a probabilistic analysis of overall exergetic efficiency to the variation of process parameters (e.g. CO_2 storage rate and compression ratio).

The thermochemical storage system shown in Figure 34 and Figure 35 is based on gas compression of CO_2 and uses existing commercial technology elements to deliver a process that satisfies energy and exergy requirements. Like the sorption based storage system described earlier, the solar reactor operates between 1 bar during dissociation and 10 bar during combination so that the heat available from the reactor is always at the same high temperature, 1200°C. This reactor operating environment demands that CO_2 must be delivered to the reactor at 10 bar pressure and is synergistic with compressed storage that stores CO_2 at pressure higher than atmospheric. In this case, if the storage and discharge from tank can be accomplished above 10 bar, then no additional compression work is required. While a high pressure is advantageous from the standpoint of reduced volume and storage cost of CO_2, there is a stiff energetic penalty in terms of compression work. A thermoeconomic optimization will be required to choose the right pressure and cost combination. Optimization may also be required in designing the overall compression process through multi-stage compression and intercooling to reduce the work input. However that will imply that the gas temperature will never be high enough to recover energy practically. At this time no such optimization has been accomplished but we have performed energy analysis at 20 bar storage pressure for CO_2 through single stage compression.

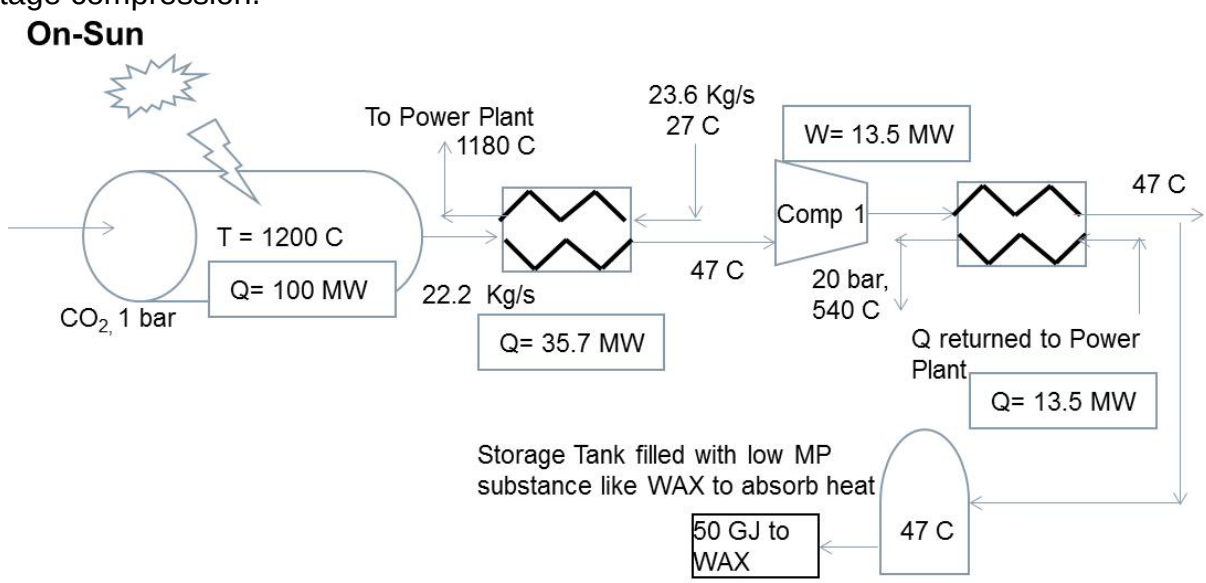

Figure 34: Schematic of the On-Sun Processes for $SrCO_3$ Dissociation

Figure 34 describes the on-sun process where the dissociated CO_2 is discharged from the reactor and is passed through a high-temperature heat-exchanger that transfers heat to the power-block. Based on a thermochemical energy storage target of 800 MW-hr and 198 kJ/mole (4.5 MJ/Kg) Heat of Reaction, 640 tonnes of CO_2 needs to be stored. For 8 hours of on-sun operation, this translates to 22.22 Kg/s of CO_2 flow at 1200 C from the reactor. The heat transferred to the power-block during on-sun hours is approximately 36 MW under these conditions.

Cooled CO_2, near room temperature, is passed into an axial compressor with a pressure ratio of 20. The discharge of this compressor is around 540°C and contains significant thermal energy which should be transferred to a power block for electricity generation (steam or supercritical CO_2) at around 40% thermal efficiency. Downstream of the heat exchanger, the pressurized CO_2 at around 47°C is discharged into a tank which has a minimum pressure of 10 bar. At the end of the on-sun period, the tank pressure rises to 20 bar as 640 tons of additional CO_2 is added. The tank volume required for this is 36000 m^3.

One should note that the CO_2 reservoir is a closed system and charging it is a dynamic process which results in increase in its temperature under adiabatic conditions. As new gas comes into the rigid walls of the reservoir, it does work on the reservoir and compresses the existing gas. If the process is adiabatic (tank is insulated or charging is fast), then this results in both temperature and pressure rise above the target temperature and pressure. This is really a rise in the internal energy of the gas. However, this is transient. If heat transfer is allowed over time, the heat will dissipate to surroundings, resulting in a penalty to the energy efficiency of the process as well as adding to exergy loss as the process is irreversible. An estimate of the heat rise using ideal gas assumption is

$$Q_{charge} = m_{sf}C_v(T_{sf} - \gamma T_i) - m_{so}C_v(T_{so} - \gamma T_i) \qquad (12)$$

Where m_{sf} is the final mass in tank, T_{sf} is final temperature in tank, m_{so} is initial mass in tank, T_{so} is initial temperature in tank and T_i is the temparature of inlet gas, γ is adiabatic exponent and C_v is specific heat of ideal gas at constant volume. In the present case T_{sf} and T_i have been assumed to be 47°C, while T_{so} is assumed to be 27°C.

While the tank returns to target pressure and temperature over time, the deficit in energy is manifested during the discharge process of the tank. As gas leaves the tank through a process of free adiabatic and irreversible expansion, it cools the tank by extracting the energy associated with work of free expansion and the pressure in the tank drops too. The final temperature in the tank will obey adiabatic law of expansion for ideal gas. This implies that the CO_2 is delivered to the reactor during the recombination phase at a temperature below storage temperature (room temperature) during substantial duration of the process.

A novel approach is suggested here to remedy the thermal dynamics of the CO_2 storage system. We suggest that the CO_2 storage tank contain paraffin wax in a way favorable to easy heat exchange with the surrounding gas and in sufficient quantity to absorb the heat generated during the charging phase as latent heat of fusion. Thus the charging is no longer an adiabatic process and the temperature of the gas will be in close equilibrium with the melting point of wax. The melting point of paraffin wax is 37°C and the energy of fusion is 200 kJ/Kg. During discharging the tank, as the temperature tends to drop below the melting point of wax, energy is transferred back to the gas to maintain

equilibrium and so that CO_2 can leave tank at approximately 300 K. In order to maintain isothermal conditions in the tank, the amount of heat required to be transferred using ideal gas assumptions is

$$Q_{discharge} = m_{sf} R T_{sf} \ln(P_{sf}/P_{so}) \qquad (13)$$

Where P_{sf} and P_{so} are the maximum and minimum pressure in the reservoir and R is the gas constant for CO_2.

Based on these assumptions, the heat required to be rejected during the tank charging process is approximately 50 GJ and that required to maintain isothermal conditions during discharging is also the same (within errors of ideal gas approximation). Based on the wax heat of fusion, this requires approximately 250 tonnes of wax, occupying a volume of roughly 250 m^3 (total tank volume of 36000 m^3).

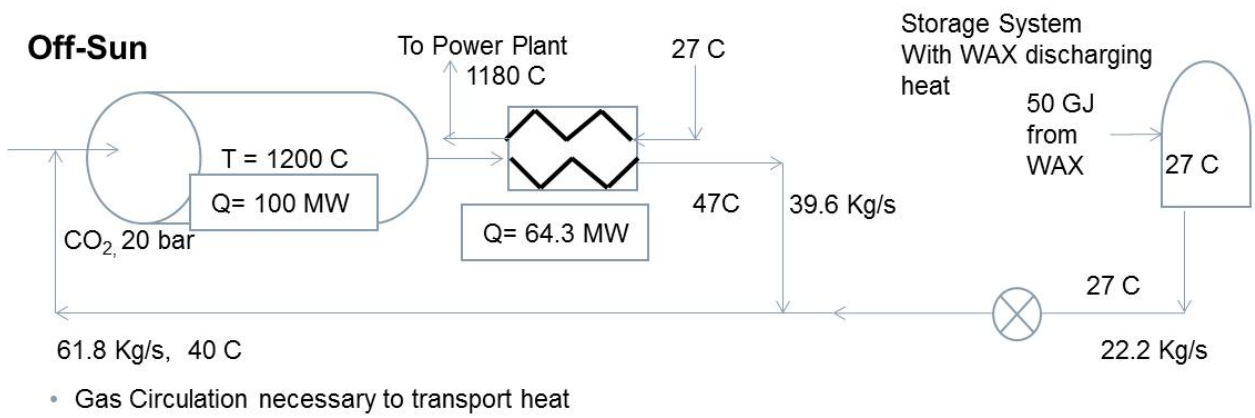

Figure 35: Schematic of Off-Sun Processes for SrCO3 Recombination.

Figure 35 shows that during the off-sun hours, CO_2 at the rate of 22.22 kg/s at a temperature of 313 K is delivered to the reactor at 10 bar. At this pressure and temperature, the reconversion to $SrCO_3$ is favored. The heat released is partially used to heat the combining CO_2 to the bed temperature. This consumes about one-third of the thermal energy released. The rest of the energy, approximately 64 MW, is carried by an additional stream of CO_2 to the power-block also at 10 bar. The pressure drop in this circuit is compensated by a low pressure rise blower not shown in the schematic. The energy consumption of this blower is small and has been neglected in the present calculation.

The exergetic calculation for the overall process (on-sun and off-sun) has been made complicated by the batch mode of operation of the system as well as a transient flow process. The approach taken here is that of identifying the irreversibilties associated with each component and summing them to derive the total exergetic loss.

The loss in exergy in the reactor during charging phase is 1.1 kJ/mole and during discharging is 4.6 kJ/mole as par chemical thermodynamics of the $SrCO_3$ system. For the compressor the loss of exergy is calculated based on the change in entropy. For the heat exchanger between the compressor and the tank, it is assumed that the heat energy is transferred to the surrounding through a work producing device operating between 540°C (nominally) and 25°C at a specified power block efficiency. The difference between this

work produced and that would have been produced via a Carnot cycle is the estimate of exergy lost.

For the charging and discharging process of the tank, the irreversibilities are due to work done on the gas remaining in the tank and work done by the gas leaving the tank. As the state of the gas remaining in the tank, is same as the state at the beginning of the charging process, all the entropy change is assumed in the working fluid. This includes the entropy change due to the change in the temperature drop in the gas during charging/discharging cycle as well as the entropy change during the expansion of discharging. For the discharging process, this analysis leads to the same conditions as isothermal expansion of a gas.

Milestone 1.5.1: The process model must demonstrate an upper bound overall exergetic efficiency, η_{ex}, of at least 90% for the TCES subsystem. This does *not* include thermal losses from the receiver/reactor, or the losses originating from the conversion of primary energy to electricity in the case of components such as pumps or compressors. A probablistic analysis will be conducted to determine the likelihood of achieving the success value based on uncertainty both in model accuracy and in the measured experimental inputs.

As the design conditions for this overall system can vary due to the technical challenges of equipment design and cost, a probabilistic assessment was performed to understand the domain of possible energy and exergy efficiency of the system. In this regard 4 design parameters – temperature pinch points in Heat Exchangers 1 and 2, Compressor efficiency and the Power Block efficiency that processes the waste heat from the gas before tank storage – were statistically varied. The quantities are varied according to “uniform distribution” and “triangular distribution”. The frequency distributions of the parameters for triangular distribution are shown in Figure 36 and Figure 37. For uniform distribution, the parameters are chosen randomly between their upper and lower limits. Table 9 shows the exergy accounting at the most probable value of each variable. Summing all the losses due to irreversibilities, the total exergy loss amounts to 465 kJ/kg. The total exergy added to the system is 5104 kJ/kg resulting in an exergetic efficiency of 0.909.

Table 9: Exergy Balance over 1 Full Cycle of Charging and Discharging.

	Exergy Added (kJ/Kg)	Exergy Destroyed (kJ/Kg)
Reactor-Charging	4500	25
Compressor	604	116
Heat Exchanger1		14
Heat Exchanger 2		149
Tank - Charging		18
Tank - Discharging		39
Reactor - Discharging		105
Total	5104	465
Exergetic Efficiency		0.909

Monte Carlo simulations were performed on the model where each parameter was selected randomly from its own distribution independent of other parameters. Several sample sizes were simulated. It was observed that there were no significant differences

in the frequency distributions between sample sizes of 1 million and 2 million for both the "uniform" and "triangular" distribution cases. Thus the 2,000,000 sample results were accepted as independent of sample size. Figure 38 through Figure 41 show the frequency distribution of the outcomes on energy and exergy efficiencies when all the parameters are randomly varied simultaneously. The results show that an exergy efficiency around 90% or greater is very likely to be possible with an energy efficiency higher than 92%. Results also show that the likely values of these efficiencies are clustered in the middle. Some of the statistics from the result distributions are shown in Table 10.

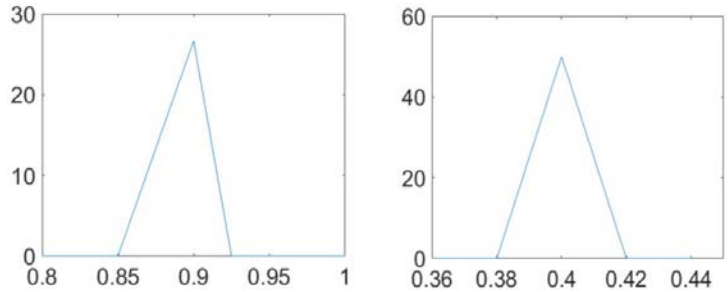

Figure 36: Triangular distribution of CO_2 compressor efficiency (left) and waste heat recovery power block efficiency (right).

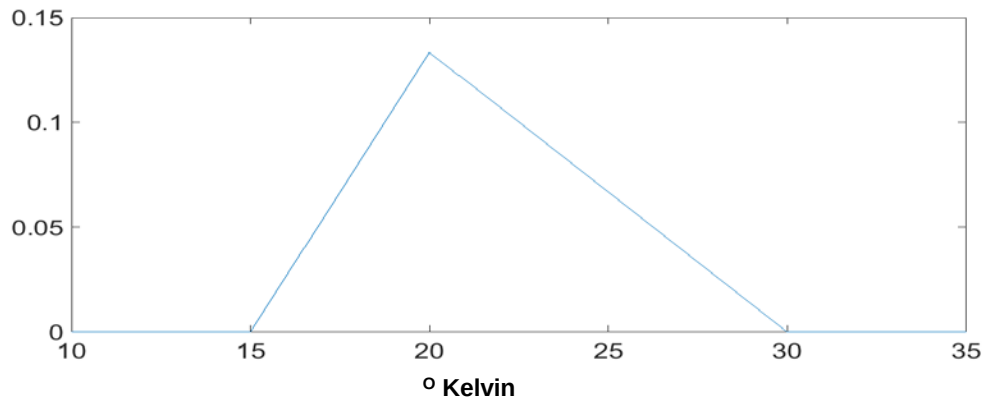

Figure 37: Triangular distribution used for heat exchanger pinch points.

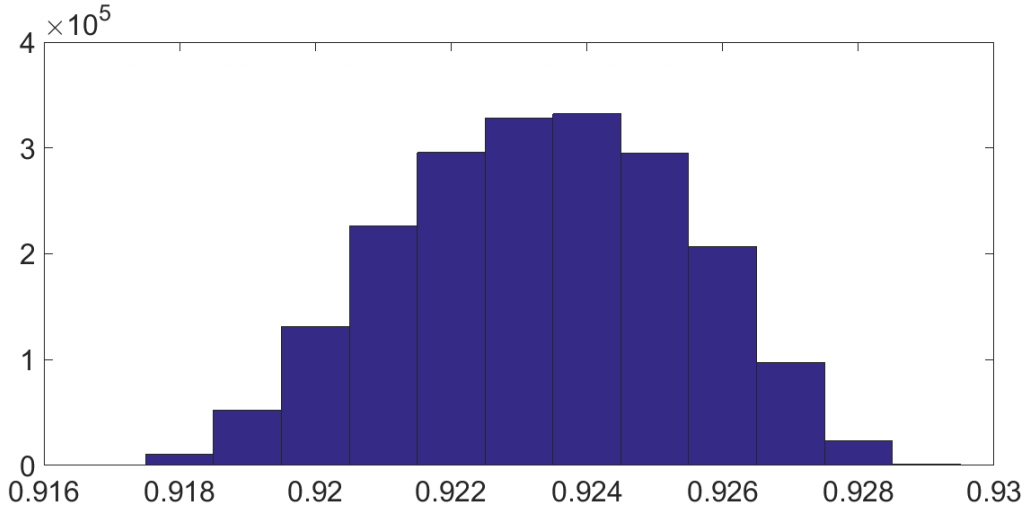

Figure 38: Energy efficiency frequency for uniform distribution of parameters.

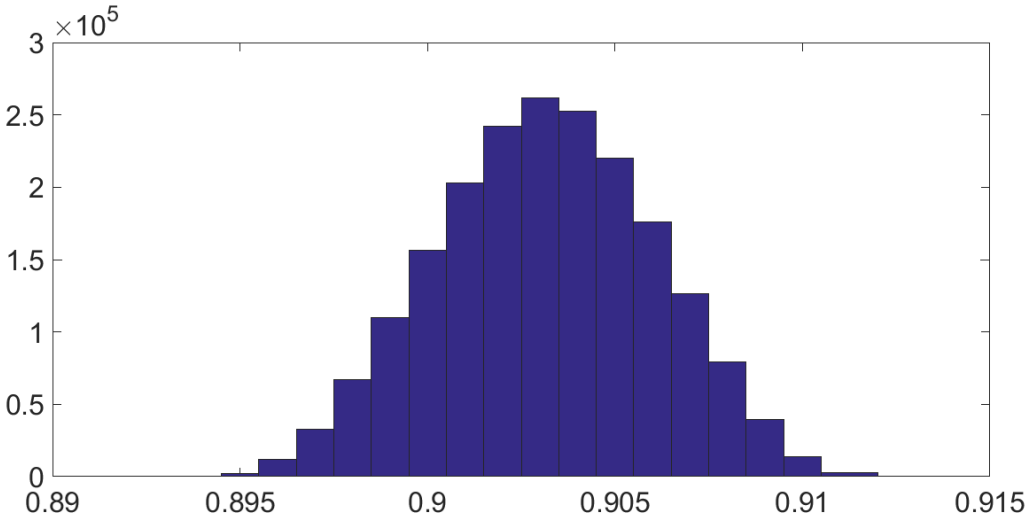

Figure 39: Exergy efficiency frequency for uniform distribution of parameters.

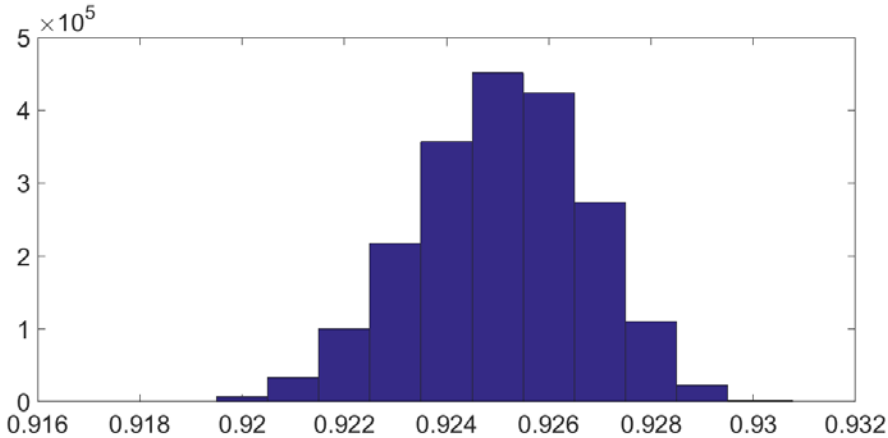

Figure 40: Energy efficiency frequency for triangular distribution of parameters.

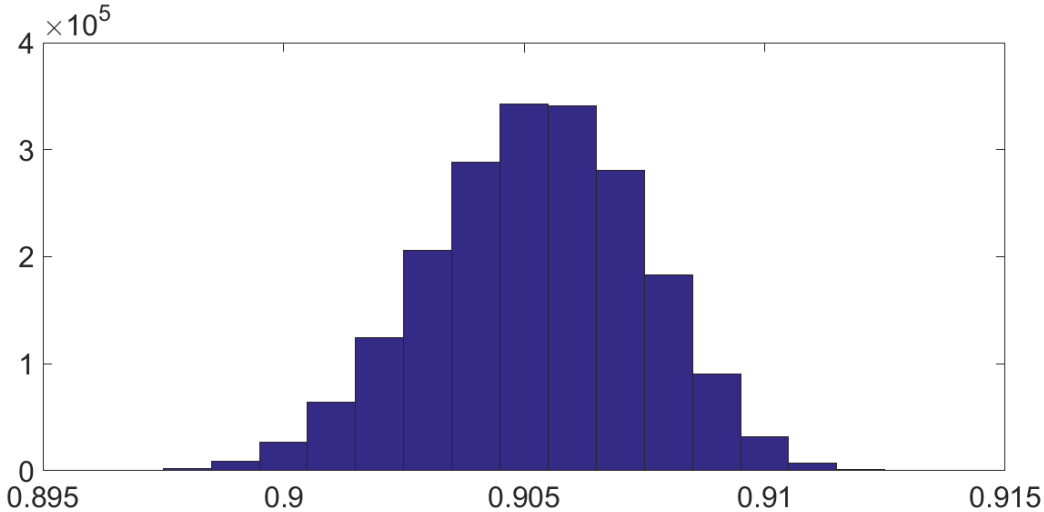

Figure 41: Exergy efficiency frequency for triangular distribution of parameters.

Table 10: Statistical results for the energy and exergy efficiencies of the proposed system subject to stochastic input parameters.

		Triangular Distribution	Uniform Distribution
Energy Efficiency	Mean	0.9251	0.9233
	Median	0.9251	0.9244
	Std. Deviation	0.0017	0.0021
	1st Quantile	0.9239	0.9218
	3rd Quantile	0.9263	0.9249
Exergy Efficiency	Mean	0.9052	0.9031
	Median	0.9053	0.9032
	Std. Deviation	0.0022	0.0029
	1st Quantile	0.9038	0.9011
	3rd Quantile	0.9068	0.9052

Pressure drop through a bed

At this stage, a specific reactor has not been designed. Based on DOE feedback, a probabilistic analysis including the additional compression work required to exceed the hypothetical pressure drop occurring through a presumed packed bed has been conducted. A triangular distribution with a minimum of 20.2, a maximum of 21, and a peak of 20.7 bar was assumed representative of a typical bed pressure drop (i.e. no more than 1 bar). Both the energy Figure 42 and exergy Figure 43 efficiency plots show minimal effect of this additional parameter compared to the base case above. This is not unexpected, as even 1 bar pressure drop is only 5% of the original compression ratio.

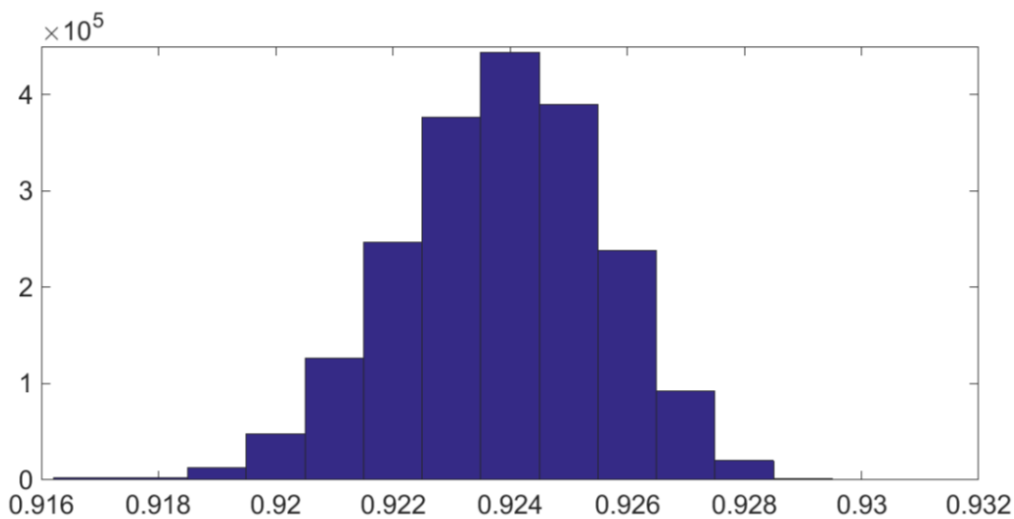

Figure 42: Energy Efficiency using triangular distribution with higher compression work.

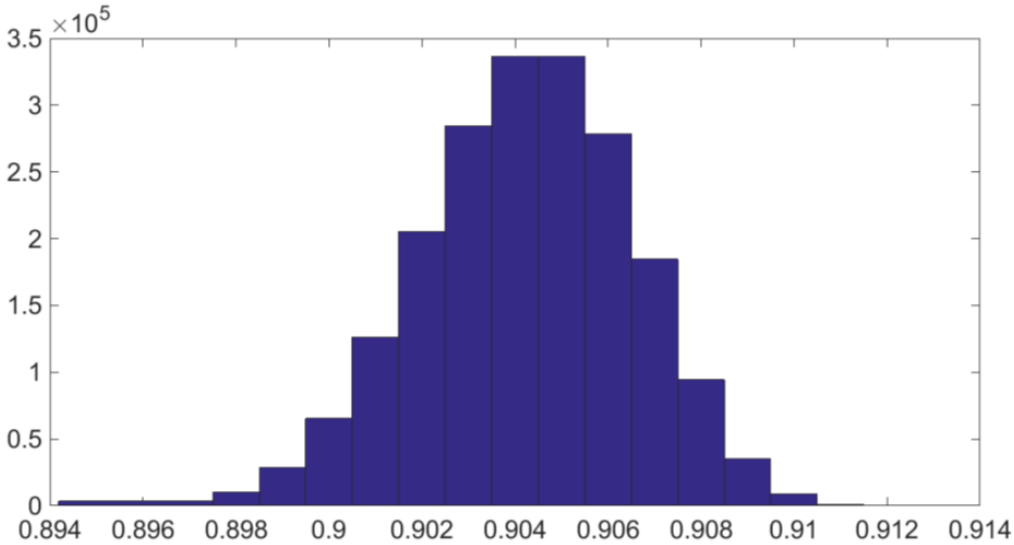

Figure 43: Exergy efficiency using triangular distribution with higher compression work.

Milestone 1.5.2: The kinetics of the carbonation reaction and CO_2 storage release allow for a peak rate of heat generation from the bed that matches 95% of the likely peak heat flow rates as determined in Milestone 1.4.2.

With this simple gas compression design, the carbonation of the bed involves simply releasing gas from the tank into the bed. The time required for gas to reach the bed is negligible compared to that of a more complicated system using a gas sorbent. Although a probabilistic analysis has not been completed for this aspect, it is anticipated that the rate is sufficient to match the 4.0 MW/m^3 benchmark.

Task 1.6: The technology to market transition will begin with formulation of a summary business plan. This plan will include: business model, summary financial model and capitalization strategy, the logical first market entry, potential strategic partners, product roadmap and key strategic milestones from which technology transfer and outreach can occur.

Subtask 1.6.1: Develop licensing option with UF for intellectual property associated with the project.

The University of Florida OTL is currently evaluating a disclosure that has been submitted by our group. Solar Fuel Corporation has a relationship with UF.

Subtask 1.6.2: Develop "Pitch" presentation for partners and to launch technology into market.

Preliminary draft of pitch is complete and following signing of NDA's, will discuss with potential partners to gain input and commercial interest.

Subtask 1.6.3: Attend at least one business-technical conference to introduce the concept on a non-confidential basis.

Given technology is still in early development with technical specifications and value proposition being clarified, we felt making a business-oriented presentation was premature and could be damaging. An appropriate conference targeting strategic operating and investment partners will be completed late summer/ fall/winter when many conferences of this nature occur.

Two technical conferences have been attended and information was shared. The conferences were the SunShot Summit 2014 and the AICHE 2014 Annual Meeting.

Subtask 1.6.4: Based on interest, compile list of potential strategic partners or potential sources of follow-on funding.

It is premature to speak in detail with business partners given stage of technology development and value proposition. As mentioned above, we have an initial draft of the presentation and we will begin discussing with potential partners beginning with the groups we are now putting NDA's in place with to conduct tests.

Milestone 1.6.1: Summary Business Plan complete, List of 6-10 potential strategic partners for future product development and go to market support. Summary business plan will include a sensitivity analysis to identify the 3 greatest cost drivers for proposed technology with a comparison to existing literature on $CaO/CaCO_3$ technologies.

Potential Strategic Partners:
We are initiating discussions with Abengoa and exploring other viable potential partners including other CSP companies as well as utilities such as Duke Energy.

Summary Business Plan
Components of the initial business plan are discussed in our partner pitch/ presentation. We are still in the early stages of developing and validating the components of the business plan and model.

Cost Drivers:

The high temperature nature of the $SrO/SrCO_3$ process results in the necessity of high temperature materials of construction. It is anticipated that the subsystem costs will be dominated by a reactor design utilizing either a robust ceramic-type material such as SiC, or a high nickel-content vessel lined with a ceramic to buffer the reactive SrO containing material. The exact magnitudes of this cost for our basis of a 100 MW system is unknown without a more specific reactor design.

The next item is a high temperature heat exchanger capable of handling hot CO_2 (ca. 1200°C) evolved from the reaction. High exergetic efficiency will require high effectiveness of the heat exchanger, which will also drive up price. A classic tradeoff between the operating costs (impacted by the efficiency) and capital investment with govern the optimization process.

Although our current exergetic efficiency estimation of approximately 90% is based on a relatively simple compression scheme, other schemes will be continue to be investigated. A sorbent scheme using either activated carbon or ionic liquids is a potential candidate. In this case, the major cost driver would be the sorbent itself, not the storage tanks. More detail on this case has been shared in the Q2 report. Due to uncertainties regarding the CO_2 solubility in the various sorbents, heats of solutions, and price, we have chosen to focus on the compression scheme at this time.

Milestone 1.6.2: Demonstrable investment of time or money in our technology from an outside entity.

We have reached or are finalizing agreements for 3 distinct outside tests to be conducted at no cost to us:

- Setaram, a thermal analysis instrumentation company, has agreed to test our material in a new prototype high pressure/high temperature TGA at their development center in France. This device will conduct carbonation at 10 bar and decomposition at 1 bar, all under an atmosphere of 100% CO_2 to best mimic realistic conditions (i.e. no dilution). The testing is tentatively scheduled for June. They have signed an NDA however the NDA was later put into revision due to complications surrounding the multi-institutional nature (UF/OSU/Solar Fuel Corporation) of the project which require several approvals.
- Setaram has also agreed to conduct thermal conductivity testing of our material. Three samples with different SrO particle sizes have been sent to Setaram's office on March 7, 2015. Thermal conductivity measurement at room temperature using their C-Therm TCi Thermal Conductivity Analyzer will be conducted with no charge.
- Netzsch, another lead thermal analysis instrumentation company, has agreed to do demonstration thermal conductivity measurement for us for free for three samples. The measurement temperature can be as high as 1100 ^{o}C using their Netzsch LFA 457 MicroFlash Laser Flash Analyzer. Three samples with different SrO particle sizes have been sent to Netzsch's office on March 3, 2015.

Conclusions:

Budget Period 1 thus far has produced a material demonstrating nearly 1000 MJ/m^3 over 100 abbreviated (i.e. 1 h carbonation) cycles. A 101st cycle was carried out to near completion (i.e. 8 h carbonation) exhibiting an energy density of approximately 1500 MJ/m^3. The project team is unaware of any other rechargeable system that can offer such an energy density at such a high temperature (ca. 1200°C). A slow but predictable decrease (0.5% per cycle) was observed over 100 cycles. Although more cycles were desired by the SOPO, 100 cycles is still a considerable demonstration of longevity, corresponding to over 3 months of charge/discharge in a solar power plant.

The peak heat flow from the system has far exceeded the goal of the SOPO Milestone 1.1.3 for the cycles carried out, in many cases by over an order of magnitude. Further longevity tests are need to determine the effect of degradation on the kinetics. Kinetic data has been gathered in tandem with DSC heat flow measurements, however an accurate model of this reversible system has yet to be finalized in according with Milestones for Tasks 1.2 and 1.3. Higher carbonation temperatures show greater extent of reaction over a 60 minute carbonation period, likely due to temperature enhanced diffusion.

Tomography images for porous $SrO/SrCO_3$ structures at initial stage and after multiple cycles have been obtained. Both 2-D and 3-D representations of the structure have been constructed. Porosity and surface area were determined from the tomography images. Permeability and Forceheimer constants in the Darcy's law have been determined from the fluid flow simulation. The thermal conductivity has been obtained from the 3-D simulations and the effect of thermal radiation at high temperature is estimated to be very small for the present structures either before or after the cycles. Computational models have been developed for predicting the energy and mass transport during the carbonation process. Many simulations have been carried out for an idealized 2-D model in order to elucidate the effects of many unknown pore scale parameters such as the diffusivity of solid on the scale of 10's of microns and the kinetics of the reaction on the particle scale. The results of the 2-D simulations show that average volumetric heat flow rate of 4 MW/m^3 in the first 5 minutes can be achieved.

A probabilistic analysis of the overall exergetic efficiency for a compression scheme coupled with storage at 20 bar has shown high likelihood of achieving 90% in fulfillment of Milestone 1.5.1. With peak power output measured in Task 1.1 at well over 40 kW/m^3, it is expected that Milestone 1.5.2 would not be of concern. Future work will focus on costing such a system.

Finally, the team has begun the process of outreach for co-development of the technology. Three distinct 3rd party tests of materials generated in Phase 1 will be conducted free of charge in the next 3-4 months. The team eagerly looks forward to ramping up dialogue with potential strategic partners in the CSP and high temperature materials field.

Budget and Schedule:

In general, we are spending according to the proposed and approved budget for the period beginning 5/1/14 and ending 4/30/15. The current balance does not reflect the

pending subcontract to Oregon State University for $45,000. We anticipate that by the end of the current budget year there will be very small balance in the account. We do not propose any change in the budget for the next year.

Although some of the milestones were met, the team fully understands that several were not. The longevity testing associated with Task 1.1 also fell short of the timeframe. The 2000 cycle milestone was a very ambitious milestone which underestimated the time required not only for carrying out 2000 cycles, but also for the material development process which is still on-going. Responsible for Tasks 1.2-1.3, Co-PI Nick AuYeung lost some time transitioning to his new institution at Oregon State but is now fully operational with a graduate student, sintering furnace, and TGA/DSC. It is anticipated that with several more weeks of model development, a suitable kinetic scheme and comparison to existing $CaO/CaCO_3$ literature can be obtained.

Path Forward:

All future tasks and Milestones are listed below. At this point, the team agrees with the plan set forward and will also finish any remaining work in Budget Period 1 (if any).

In addition to the previously agreed activities, the team plans to continue fundamental material studies:

- ***Characterization of the potential additional heat storage occurring from solid-solid transition(s).*** This will impact process design and potentially increase the energy density significantly. Although such a temperature dependent energy release will require some significant process consideration for utilization in a real CSP system, this additional energy storage could be an enormous boom to the value proposition. Although the team suspects that $SrZrO_3$ has a distinct solid transition ca. 1170°C, the active $SrO/SrCO_3$ material has some high temperature phase transitions as well. A series of controlled experiments using DSC at slow ramp rates will be carried out to resolve these events.
- ***Exploration of synthesis techniques.*** Synthesis of supported SrO materials has largely used solid state sintering techniques. In Phase 2, wet chemical synthesis such as co-precipitation will be used to create more homogeneous materials. Better distributed materials can be significantly longer lasting and more productive.
- ***Simulation of TGA-scale reaction to determine intrinsic kinetic parameters.*** Data obtained is largely an average value of the reaction extent of the entire material, whereas in reality the surface and bulk reaction extent may be significantly different.

References:

[1] J. Stekli, L. Irwin and R. Pitchumani, Journal of Thermal Science and Engineering Applications, 2013, 5, 021011-021011.
[2] G. Ervin, Journal of Solid State Chemistry, 1977, 22, 51-61.
[3] R. Dunn, K. Lovegrove and G. Burgess, Proceedings of the IEEE, 2012, 100, 391-400.
[4] B. Wong, L. Brown, R. Buckingham, D. Thomey, M. Roeb and C. Sattler, in SolarPACES 2012, Marrakech, Morocco, 2012.
[5] D. N. Harries, M. Paskevicius, D. A. Sheppard, T. E. C. Price and C. E. Buckley, Proceedings of the IEEE, 2012, 100, 539-549.
[6] D. A. Sheppard, C. Corgnale, B. Hardy, T. Motyka, R. Zidan, M. Paskevicius and C. E. Buckley, RSC Advances, 2014, 4, 26552-26562.
[7] S. E. B. Edwards and V. Materic, Solar Energy, 2012, 86, 2494-2503.
[8] Y. Kato, T. O-shima and Y. Yoshizawa, International Journal of Energy Research, 2001, 25, 577-589.
[9] M. Kubota, K. Kyaw, F. Watanabe, H. Matsuda and M. Hasatani, Journal of Chemical Engineering of Japan, 2000, 33, 797-800.
[10] Y. Kato, D. Saku, N. Harada and Y. Yoshizawa, Journal of Chemical Engineering of Japan, 1997, 30, 1013-1019.
[11] M. S. Murthy, P. Raghavendrachar and S. V. Sriram, Solar Energy, 1986, 36, 53-62.
[12] R. Barker, Journal of Applied Chemistry and Biotechnology, 1974, 24, 221-227.
[13] M. Aihara, T. Yoshii, Y. Shimazaki, T. Takeuchi and H. Habuka, Journal of Chemical Engineering of Japan, 2008, 41, 513-518.
[14] M. Zhao, J. Shi, x. Zhong, S. Tian, J. Blamey, J. Jiang and P. Fennell, Energy & Environmental Science, 2014.
[15] L. Reich, L. Yue, R. Bader and W. Lipinski, Aerosol and Air Quality Research, 2014, 14, 500-514.
[16] E. Mostafavi, M. H. Sedghkerdar and N. Mahinpey, Industrial & Engineering Chemistry Research, 2013, 52, 4725-4733.
[17] W. Liu, H. An, C. Qin, J. Yin, G. Wang, B. Feng and M. Xu, Energy & Fuels, 2012, 26, 2751-2767.
[18] S. P. Wang, S. L. Yan, X. B. Ma and J. L. Gong, Energy & Environmental Science, 2011, 4, 3805-3819.
[19] H. Chen, C. Zhao, Y. Li and X. Chen, Energy & Fuels, 2010, 24, 5751-5756.
[20] H. Chen, C. Zhao and W. Yu, Applied Energy, 2013, 112, 67-74.
[21] N. Rong, Q. Wang, M. Fang, L. Cheng, Z. Luo and K. Cen, Energy & Fuels, 2013.
[22] L. Rouchon, L. Favergeon and M. Pijolat, Journal of Thermal Analysis and Calorimetry, 2013, 113, 1145-1155.
[23] Z. Zhou, Y. Qi, M. Xie, Z. Cheng and W. Yuan, Chemical Engineering Science, 2012, 74, 172-180.
[24] F.-C. Yu and L.-S. Fan, Industrial & Engineering Chemistry Research, 2011, 50, 11528-11536.
[25] W. Liu, B. Feng, Y. Wu, G. Wang, J. Barry and J. C. D. da Costa, Environmental Science & Technology, 2010, 44, 3093-3097.
[26] B. Yu, P. Zhang, L. Zhang, J. Chen and J. Xu, Science in China Series B-Chemistry, 2008, 51, 878-886.
[27] C. Qin, W. Liu, H. An, J. Yin and B. Feng, Environmental Science & Technology, 2012, 46, 1932-1939.
[28] A. M. Kierzkowska, R. Pacciani and C. R. Mueller, Chemsuschem, 2013, 6, 1130-1148.

[29] M. Kubota, K. Kyaw, F. Watanabe, H. Matsuda and M. Hasatani, Journal of Chemical Engineering of Japan, 2001, 34, 326-332.
[30] A. Wolfgang and P. Wasserscheid, Patent number: DE102010009543-A1, Germany, 2011.
[31] Valverde, J.M., Sanchez-Jimenez, P.E., and Perez-Maqueda, L.A., 2014, “High and stable CO2 capture capacity of natural limestone at Ca-looping conditions by heat pretreatment and recarbonation synergy,” Fuel, 123, pp. 79-85.
[32] Valverde, J.M., Sanchez-Jimenez, P.E., and Perez-Maqueda, L.A., 2014, “Effect of heat pretreatment/recarbonation in the Ca-looping process at realistic calcination conditions,” Energy & Fuels, 28 (6), pp. 4062–4067.
[33] Bhatia, S. K., and Perlmutter, D. D., 1983, "Eeffect of the product layer on the kinetics of the CO_2-lime reaction," AIChE Journal, 29(1), pp. 79-86.
[34] Rouchon, L., Favergeon, L., and Pijolat, M., 2013, "Analysis of the kinetic slowing down during carbonation of CaO by CO_2," Journal of Thermal Analysis and Calorimetry, 113(3), pp. 1145-1155.
[35] deLigny, D., and Richet, P., 1996, "High-temperature heat capacity and thermal expansion of $SrTiO_3$ and $SrZrO_3$ perovskites," Physical Review B, 53(6), pp. 3013-3022.
[36] Charsley, E. L., Earnest, C. M., Gallagher, P. K., and Richardson, M. J., 1993, "Preliminary round-robin studies on the ICTAC certified reference materials for DTA-Barium carbonate and strontium carbonate," Journal of Thermal Analysis, 40(3), pp. 1415-1422.
[37] Gürsoy D., De Carlo F., Xiao X., and Jacobsen C., 2014, “TomoPy: a framework for the analysis of synchrotron tomographic data,” Journal of Synchrotron Radiation, 21(5), pp. 1188–1193.
[38] Singh, B. P., and Kaviany, M., 1992, “Modelling radiative heat transfer in packed beds,” Int. J. Heat Mass Transf., 35(6), pp. 1397–1405.
[39] Kamiuto, K., Iwamoto, M., Sato, M., and Nishimura, T., 1991, “Radiation-extinction coefficients of packed-sphere systems,” J. Quant. Spectrosc. Radiat. Transf., 45(2), pp. 93–96.
[40] Hendricks, T., Howell, J. "Absorption/scattering coefficients and scattering phase functions in reticulated porous ceramics," ASME Journal of Heat Transfer, 118:79– 87, 1996.
[41] Szelagowski, H., Arvanitidis, I., and |Seetharaman, S., 1999, “Effective thermal conductivity of porous strontium oxide and strontium carbonate samples,” J. Applied Physics, 85, pp. 193-198.
[42] Ackermann, S., Scheffe, J., Duss, J., and Steinfeld, A., 2014, “Morphological Characterization and Effective Thermal Conductivity of Dual-Scale Reticulated Porous Structures,” Materials, 7, pp. 7173–7195.
[43] Bohn, C. D., Scott, S. A., Dennis, J. S., and Mueller, C. R., 2012, "Validation of a lattice Boltzmann model for gas-solid reactions with experiments," Journal of Computational Physics, 231(16), pp. 5334-5350